Mettl5 coordinates protein production and degradation of PERIOD to regulate sleep in *Drosophila*

Xiaoyu Wu[1#], Xingzhuo Yang[1#], Tiantian Fu [1#], Yikang S. Rong[2], Juan Du[1*]

1 State Key Laboratory of Agricultural and Forestry Biosecurity, MOA Key Lab of Pest Monitoring and Green Management, Department of entomology, College of Plant Protection, China Agricultural University, Beijing 100193, China

2 MOE Key Lab of Rare Pediatric Diseases, Hengyang College of Medicine, University of South China, Hengyang, China

[*]Correspondence author: Juan Du, dujuan9981@cau.edu.cn

[#] These authors contribute equally to this work.

Summary

Sleep plays a critical role in animal physiology, primarily governed by the brain, and its disruption is prevalent in various brain disorders. Mettl5 is associated with intellectual disability (ID), which often includes sleep disturbances. However, the mechanism underlying these sleep disruptions in ID remains poorly understood. In this study, we investigated the sleep phenotypes resulting from *Drosophila Mettl5* mutations. Rescue experiments revealed that *Mettl5* functions predominantly within neurons and glia marked by *Mettl5*-Gal4 to regulate sleep. Previous work established that Mettl5 forms a complex with Trmt112 to influence rRNA methylation. Notably, a mutation in *Trmt112* mutation recapitulated these sleep disturbances, implicating translational regulation by the Mettl5/Trmt112 complex. Subsequent RNA-seq and Ribo-seq analyses of *Mettl5*^{1bp} mutants uncovered downstream effects, including altered expression of proteasome components and clock genes. Rescue experiments confirmed that the net increase in PERIOD protein underlies the sleep phenotype. This study illuminates the interplay between ribosome function, clock genes, and the proteasome in sleep regulation, highlighting the integrated roles of protein synthesis and degradation. These findings could potentially provide an example for *in vivo* study of rRNA methylation function, expand our understanding of protein homeostasis in sleep and offer insights into the sleep phenotypes associated with ID.

Key words: *Mettl5*, rRNA methyltransferase, proteasome, Clock genes, sleep

Introduction

Sleep is essential for animal physiology, and understanding its molecular mechanisms has significant implications for both basic research and clinical applications. Although previous studies have identified key sleep regulators (*Du et al., 2021*), fundamental questions remain regarding the roles of cellular processes such as protein synthesis and degradation in sleep regulation.

Growing evidence suggests a dynamic interplay between sleep regulation and protein homeostasis. Protein synthesis is particularly active during sleep (*Lyons et al., 2023*), while Sleep deprivation affects translational initiation (*Costa et al., 2019*). The proteasome, a critical mediator of ubiquitin-dependent protein degradation, regulates synapse homeostasis by modulating ribosomal components (*Costa et al., 2019*), thereby influencing synaptic function. Intriguingly, proteasome components exhibit oscillating expression pattern at the transcriptional level in human cells (*Desvergne et al., 2016*). A recent study in *Drosophila* showed that mutation in a proteasome component alters sleep patterns (*Fernández et al., 2020*). Despite these advances, the precise mechanisms by which protein synthesis and degradation influence sleep, and how these processes interact, remain unresolved.

While several factors influencing proteasome assembly and subunit transcription have been identified (*Kapetanou et al., 2022*), the translational control of proteasome subunits remains poorly understood. Additionally, proteasome inhibition has been shown to alter ribosome function (*Galimberti et al., 2016; Costa et sl., 2019; Palanca et al., 2014*), raising the question of whether the proteasome itself is regulated by the status of the translation machinery. Exploring this relationship could provide key insights into the interplay between proteasome activity and translation.

In *Drosophila*, *Mettl5* exhibits 18S ribosomal RNA m^6A methyltransferase activity (*Leismann et al., 2020*) and interacts with Trmt112 to facilitate this function, a mechanism conserved in human (*Leismann et al., 2020; van Tran et al., 2019*). Although *Mettl5* depletion abolishes m^6A modification on 18S rRNA without impairing rRNA maturation, it affects fly orientation behavior. In mammalian cells, *Mettl5*-mediated 18S rRNA N6-methyladenosine (m^6A) modification regulates stem cell fate determination and neural function (*Wang et al.*, *2020*). However, it remains unclear whether *Mettl5* modulates global or transcript-specific translation profile *in vivo*, particularly in tissues rather than cell lines. Moreover, while *Mettl5* is linked to intellectual disability (ID) with comorbid sleep disturbances,

its mechanistic role in these disorders is unknown. Testing whether *Mettl5* loss affects behaviors like sleep in *Drosophila* could clarify this connection.

We discovered that *Mettl5* regulates sleep in *Drosophila*. To investigate the underlying mechanism, we performed RNA-seq and Ribo-seq on *Mettl5* mutants, revealing dysregulation of multiple clock genes and proteasome components. This suggests *Mettl5* coordinates protein production and degradation, which are crucial for protein homeostasis. Follow-up experiments confirmed that the protein level of Period was upregulated in *Mettl5* mutants, contributing to the sleep phenotype. This study highlights that ribosome defects can perturb proteasome function, uncovering a mechanism that couples protein degradation with synthesis. Additionally, by mapping the genome-wide downstream gene profile of an rRNA methylation modifier, this study offers insights into the gene-specific roles of ribosome function.

Results

Mettl5 regulates sleep in *Drosophila*

Mettl5 contains a predicted N6 adenine specific nucleic acids methyltransferase domain. In order to study the function of this gene in sleep regulation, we generated CRISPR-Cas9 knockout mutants. We created two alleles. $Mettl5^{1bp}$, which deleted 1bp in the coding region results in a truncated version (Figure 1A) and down regulation of *Mettl5* at mRNA level (Figure 1B). Another allele $Mettl5^{9bp}$, which results in 3 amino acids deleted version of *Mettl5* (Figure 1A) does not cause significant change at mRNA level (Figure 1B). We found that heterozygous $Mettl5^{1bp}$ mutants exhibited significantly reduced nighttime sleep (Figure 1C-G), particularly during early night (ZT12-ZT16; Figure 1C). Quantitative analysis revealed increased wakefulness at ZT14 in mutants (Figure 1H). 'awake %' was used to indicate the percentage of awake fruit fly population at specific time points (e.g., ZT14). quantitative nighttime sleep latency measurements indicated a delayed sleep start in mutants (Figure S1G). In addition, *Mettl5* expression was significantly up regulated during the sleep recovery period after mechanical sleep deprivation (Figure 1I-J). *Mettl5* mutant displayed significantly increased sleep rebound in 24 hours after sleep deprivation (Figure 1K-L), indicating its effects on sleep homeostasis. Moreover, results of sleep arousal assay at ZT19 indicated that the percentage of aroused flies are significantly more than the control group (Figure 1M). These results demonstrate that the truncated

Mettl5 mutation causes sleep deficits, establishing *Mettl5* as a novel sleep regulator in *Drosophila*.

To confirm the specificity of the sleep phenotype in *Mettl5*^{1bp}, we performed genetic rescue experiments. Introduction of a single wild-type *Mettl5* copy completely rescued both the reduced sleep amount and increased wakefulness at ZT14 (Figure 1N-R), demonstrating that these phenotypes specifically result from *Mettl5* deficiency.

The observed expression pattern of *Mettl5* further supports its sleep regulatory function. Using *Mettl5*-Gal4 reporter lines, we found expression in both neurons (colocalizing with ELAV staining; Figure S1A-C) and glial cells (colocalizing with Repo staining; Figure S1D-F). Behavioral analyses revealed additional mutant phenotypes consistent with sleep dysregulation. we tested the climbing ability of *Mettl5* mutation which showed an increase (Figure S1H). RNAi knocking down of *Mettl5* showed a consistent phenotype of down regulated sleep amount during the night time (Figure S1I-L).

Mettl5 regulates _Drosophila_ sleep through its methyltransferase activity

Previous studies established that Mettl5 interacts with Trmt112 to regulate 18S rRNA m^6A modification (*Leismann et al., 2020; van Tran et al., 2019*). Consistent with these findings, our LC-MS/MS analysis revealed significantly reduced m^6A levels in both total RNA and 18S rRNA from heterozygous *Mettl5*^{1bp} (Figure 2A-B). To determine whether Mettl5's sleep regulatory function depends on its methyltransferase activity, we performed two key experiments. First, we examined the phenotype of *Trmt112* knockdown. We found that the *Mettl5*-Gal4 driven *Trmt112* RNAi resulted in a similar phenotype to *Mettl5*^{1bp} (Figure 2C-G), suggesting that *Mettl5* regulates sleep through its 18S rRNA m^6A modification activity. The efficiency of the *Trmt112* RNAi line was tested in previous study (*López-Varea et al., 2021*). More important, we performed a rescue experiment with a mutated form of *Mettl5* that lacks the NPPF amino acids required for its methyltransferase activity (Figure2A) (Iyer et al., 2016). We observed that this mutant *Mettl5* failed to rescue the sleep phenotype caused by *Mettl5*^{1bp} (Figure 2H-L). Together, these results demonstrate that Mettl5's methyltransferase activity is essential for its role in sleep regulation, likely through its function in 18S rRNA m^6A modification.

RNA-seq and Ribo-seq revealed the downstream gene profile of _Mettl5_

To better understand the downstream events of *Mettl5*, we performed RNA-seq and Ribo-seq to assess transcriptomic and translational changes in *Mettl5*^{1bp}. Principal Coordinates Analysis (PCoA)

of RNA-seq and Ribo-seq datasets revealed clear separation between mutant and control groups (Figure S2A, B, D, E). High reproducibility was found among biological replicates (Figure S2C, F), confirming data quality. Transcriptome analysis identified 1,053 significantly differentially expressed genes ($|\log_2 (\text{Fold Change})| \geq 1$ & $p^{adj} < 0.05$), comprising 217 upregulated and 836 downregulated transcripts (Figure 3A, B). Parallel ribosome profiling revealed 299 translationally regulated genes ($|\log_2 (\text{Fold Change})| \geq 0.265$ & $p^{adj} < 0.05$), with 149 upregulated and 150 downregulated targets compared to the controls (Figure 3C). Heatmaps of the top 100 differentially expressed genes from both RNA-seq and Ribo-seq analyses were generated according to the rlog transformed values (Figure S3A, B).

To explore the biological implication of differentially expressed genes at transcriptional and translational levels, we performed Gene Ontology (GO) enrichment analysis. At the transcriptional level (Figure S4A, C), the most significantly enriched biological processes included cellular response to chemical stimulus, small molecule biosynthetic process, and fatty acid metabolic process (Figure S4A), with supporting gene networks (Figure S4C). Translational-level analysis (Figure S4B, D) revealed prominent enrichment for organic acid and amino acid metabolic processes, lipid catabolism, cellular respiration, and transport mechanisms. Notably, we identified strong associations with circadian regulation, including circadian regulation of gene expression and entrainment of the circadian clock.

The GO results usually contain a long list of enriched terms that have highly redundant information and are difficult to summarize. So, we performed a simplify Enrichment analysis that visualizes the summaries of clusters by word cloud for the GO enrichment result at transcriptional and translational levels. For transcriptionally significant DEGs (Figure S5A), major enriched processes included metabolic and stimulus-response pathways, wing disc and imaginal system development, ion-channel homeostasis and transport, and cytokinesis/cell cycle transitions. Translationally regulated genes additionally showed enrichment for sleep-wake cycles, circadian behavior, and neuronal cell death (Figure S5D). Cellular component analysis highlighted chromosomal structures, membrane-bound complexes, and vesicles (Figure S5B), while molecular functions predominantly involved enzymatic activities, ion/protein binding, receptor activities, and transcription processes (Figure S5C).

The strong concordance between RNA-seq and Ribo-seq enrichment profiles (Figure S5E-F) further validated these findings.

Our Gene Set Enrichment Analysis (GSEA) identified pathways enriched in differentially expressed genes at both transcriptional and translational levels. To capture subtle but biologically important changes that might be excluded by stringent statistical thresholds, we analyzed gene sets ranked by log2 fold-change without p-value filtering. The GSEA-GO and GSEA-KEGG results, sorted by Normalized Enrichment Score (NES), revealed several key pathways (Figure S6A-D). Notably, the proteasome pathway showed significant suppression at both transcriptional and translational levels (P.adjust<0.05) (Figure 3E, I). Transcriptional-level analysis highlighted disruptions in arginine and proline metabolism and insect hormone biosynthesis (P.adjust<0.05) (Figure 3D, G). While, while translational changes predominantly affected fatty acid degradation and phosphonate/phosphinate metabolism (P.adjust<0.05) (Figure 3H-K).

To better understand the correlation between transcription and translation levels, we performed correlation analysis of differentially expressed genes based on fold change of DEGs (Figure 3L). 977 genes showed opposing trends between transcription and translation, while only 24 genes exhibited concordant changes. We identified 240 translation-specific and 3,309 transcription-specific DEGs, with each cluster undergoing separate enrichment analysis (Figure S7A-H). Notably, core clock genes (*Clk*, *tim*, etc.) displayed significant changes at both levels (Figure 3L).

To isolate translational effects, we calculated translation efficiency (TE) differences between *Mettl5*^{1bp} and *w*^{1118} controls (Figure 3M). Among 1,204 genes with significantly altered TE, GO enrichment highlighted amino acid metabolism and small molecule biosynthesis (Figure 3N), while KEGG analysis emphasized glycine/serine/threonine metabolism and one-carbon pool by folate pathways (Figure 3O, P).

Ribo-seq revealed the *Mettl5*^{1bp} led to changes of some global translation features

Using Ribo-seq, we compared global translation features between the *w*^{1118} and *Mettl5*^{1b} groups. The TE (translation efficiency) correlation coefficients among the three biological replicates of each genotype ranged from 0.87 to 0.93, demonstrating high reproducibility within genotypes (Figure S8A-F). We found that the length of ribosome-protected RNA fragments (RPFs) was approximately 28nt

169 (Figure S10A). The RPFs exhibited a significant 3-nt periodicity. Metagene analysis of individual 28nt
170 reads revealed the distribution of RPFs across the gene locus in w^{1118} and $Mettl5^{1bp}$, respectively (Figure
171 S8, S9). The starting point of translation is 12nt upstream of start-codon and gradually disappears 15nt
172 from stop-codon (Figure S8G-L). RPFs on the metagene plot distribution around the translation start
173 and translation stop site (Figure S9A-F), different coding frames on CDS, 3'-UTR and 5'-UTR,
174 respectively in two groups of samples all showed the periodicity (Figure S9G-L). As expected, all
175 plots show an enrichment of P-sites in the first frame on the coding sequence but not the UTRs, in
176 accord with ribosome protected fragments from protein coding mRNAs (Figure S9G-L).

177 Analysis of open reading frame (ORF) types revealed alterations in their distribution. Compared
178 to w^{1118}, $Mettl5^{1bp}$ exhibited an increased proportion of overlapping downstream ORFs (dORFs) and
179 fewer non-overlapping dORFs (Figure S10B). In both groups, translated upstream ORFs (uORFs)
180 were significantly shorter than untranslated uORFs ($P < 0.05$) (Figure S10C).
181 Additionally, $Mettl5^{1bp}$ displayed reduced read counts for both dORFs and uORFs (Figure S10D-E).
182 Based on translation potential, uORFs were classified as either translated or untranslated, and motif
183 analysis was performed separately for each category (Figure S10F-G).

184 Mutation of *Mettl5* altered codon preference

185 Comparison of codon occupancy (A-site) between the two groups revealed
186 that *Mettl51bp* preferentially used GAC and GAU, whereas *w1118* favored UCC (Figure S10H). This
187 trend was further supported by the cumulative frequency distribution of these codons (Figure S10I-K).
188 Since GAC and GAU both encode aspartate (Asp), we analyzed Asp amino acid occupancy.
189 Intriguingly, Asp was significantly enriched in *w1118* during translation (Figure S10L), suggesting
190 that *Mettl51bp* may exhibit altered translational regulation (see Discussion for details).

191 Metagene analysis of RPFs revealed distinct translation patterns between $Mettl5^{1bp}$ and w^{1118}. The
192 coding sequence (CDS) and flanking regions were segmented into 100 equal bins, and average RPF
193 density was computed for each bin. The resulting plots illustrate differences in ribosome occupancy
194 between $Mettl5^{1bp}$ and w^{1118} along the CDS (Figure S10M), near the translation start site (Figure S10N)
195 and around the translation termination site (Figure S10O). Notably, $Mettl5^{1bp}$ and w^{1118} exhibited
196 divergent ribosome occupancy patterns, particularly along the CDS and near the start codon (Figure

197 S10M, N), suggesting potential differences in translation dynamics and initiation efficiency.

198 ***Mettl5* regulates the clock gene regulatory loop**

199 Our findings demonstrate that *Mettl51bp* disrupts the core clock gene regulatory loop controlling
200 circadian rhythm. We observed significant alterations in both transcriptional and translational levels
201 of multiple clock genes, with *Cry* and *Clock* showing upregulation while *Tim*, *per*, *vri*, and *pdp1* were
202 downregulated at both levels (Figure 4A-B). Notably, *per*, *vri*, and *pdp1* exhibited particularly
203 pronounced downregulation in translation efficiency (Figure 4C). These changes occurred without
204 affecting clock neuron morphology at different time points (Figure S11).

205 The observed expression patterns revealed an unexpected regulatory relationship: while the
206 canonical clock circuitry positions *Per* downstream of *Clock*, our finding that *Clock* was upregulated
207 while *per* was downregulated suggests *Per* may actually function upstream of *Clock* in *Mettl5*-
208 mediated regulation. Surprisingly, despite the transcriptional downregulation of *per* (Figure 4D), we
209 detected increased PER protein levels through both immunostaining and western blot analyses (Figure
210 4E-H). Detection of the PER protein at different time points indicated that it was increased at both ZT
211 0 and ZT18 (Figure 4E-F). This apparent contradiction aligns with the observed circadian phenotype,
212 as *Mettl5* mutants showed significantly longer period lengths (Table 1), mirroring effects seen when
213 PER stabilization results from reduced kinase activity as previously reported (Philpott et al., 2023).
214 Genetic epistasis experiments further supported this model, with double mutants exhibiting clock gene
215 phenotypes that position both *Clock* and *Per* downstream of *Mettl5* (Figure 4I-N, Table 1). Together,
216 these results indicate that $Mettl5^{1bp}$ affects circadian regulation through mechanisms that extend
217 beyond transcriptional control, likely involving post-translational regulation of PER protein stability.

218 To investigate the factors mediating PER protein level changes in *Mettl5* mutants, we examined
219 the ubiquitin-proteasome pathway, which plays a well-documented role in Period protein degradation
220 (Grima et al., 2002; Ko et al., 2002; Chiu et al., 2008). Notably, recent evidence indicates that N6-
221 methyladenosine (m6A) regulates the ubiquitin-proteasome system in other biological contexts (Sun
222 et al., 2023). Our integrated analysis of RNA-seq and Ribo-seq data revealed significant
223 downregulation of multiple proteasome pathway components in $Mettl5^{1bp}$ mutants at both
224 transcriptional and translational levels (Figures 3E, 3I, 4O), suggesting impaired protein degradation

capacity. Based on these findings, we propose a model where *Mettl5* regulates circadian function through three interconnected mechanisms: first, by directly modulating proteasome components to control PER protein stability post-translationally; second, by transcriptionally and translationally regulating Per and other clock expression. In this model, *Mettl5*^{1bp}-induced proteasome downregulation leads to PER accumulation, which is responsible for the phenotypes (Figure 5).

Mettl5^{1bp} alters axon complexity

Previous studies have established a strong correlation between sleep homeostasis and synaptic complexity (Bushey et al., 2011). Additionally, synaptogenesis has been shown to enhance proteasome activity in axons (Costa et al., 2019). Given our observations of impaired sleep rebound following deprivation and altered expression of proteasome subunits in *Mettl5*^{1bp} mutants, we sought to examine potential effects on synaptic complexity.

To assess synaptic complexity, we adapted an established quantification method (Bushey et al., 2011) using Syt-GFP, a marker that colocalizes with endogenous synaptic vesicles, to visualize presynaptic morphology changes. Control experiments with UAS-*Fmr1* and *Fmr1* mutations successfully replicated the expected decrease and increase in syt-eGFP signal, respectively (Figure 6A-D). Strikingly, *Mettl5*^{1bp} mutants exhibited significantly increased syt-eGFP fluorescence in presynaptic terminals (Figure 6E-M), indicating altered synaptic complexity.

Discussion

Our study reveals that Mettl5, a known rRNA methyltransferase, modulates sleep through its RNA methylation activity. Through integrated RNA-seq and Ribo-seq analyses of *Mettl5*^{1bp} mutants, we identified *Mettl5*'s downstream targets at both transcriptional and translational levels. Further investigation demonstrated that Mettl5 influences sleep regulation by affecting two key pathways: the circadian clock gene network and the proteasome system. These findings provide novel mechanistic insights into sleep control, highlighting the coordinated role of protein synthesis and degradation in this process. Notably, our Ribo-seq analysis revealed that *Mettl5*^{1bp} alters fundamental translation features, including uORF translation efficiency and codon preference, suggesting rRNA methylation plays a regulatory role in these processes.

This discovery has important clinical implications, as METTL5, the human ortholog of Mettl5, is

associated with intellectual disability (ID) when mutated (Richard et al., 2019). Our work expands the understanding of Mettl5's molecular function and may inform potential therapeutic strategies for ID. The clinical relevance of our findings is underscored by reports of sleep disturbances, particularly reduced sleep duration, in ID patients - a phenotype that parallels our observations in *Mettl5*^{1bp} mutants. The mechanistic framework established in this study could explain these clinical sleep abnormalities. However, further validation in vertebrate models is needed to determine whether this regulatory mechanism is evolutionarily conserved and applicable to human sleep disorders.

As shown in Table 1, the *Mettl5*^{1bp}/+ mutant exhibits a robust long-period phenotype, with circadian rhythms significantly extended to 28.3 ± 0.4 hours compared to the wild-type's 23.9 ± 0.05 hours. This prolonged period perfectly aligns with the observed behavioral phenotypes, including delayed nighttime sleep onset, later daytime waking, and the overall shift in sleep profile. This is indeed quite similar to previous report on Period3 variant (*Zhang et al., 2016*). We think that the prolonged circadian period contributes to the observed sleep phenotype. However, since total sleep time was significantly reduced in the mutant, we cannot attribute the phenotype solely to period lengthening. Furthermore, our 24-hour PER expression analysis in *Mettl5* mutants revealed elevated PER protein levels at ZT1 and ZT18, while ZT6 and ZT12 showed no significant changes, with no apparent phase shift. These findings collectively suggest that the phenotype primarily results from PER protein stabilization and accumulation.

We found that *Mettl5* heterozygotes showed significant reductions in total RNA and 18S rRNA methylation levels, contrasting with mouse studies where heterozygous knockouts maintained normal 18S rRNA m6A methylation (*Sepich-Poore et al., 2022*). This discrepancy may stem from either fundamental differences in rRNA methylation regulation between *Drosophila* and mice, or distinct biological consequences of knockdown versus knockout approaches, as complete gene elimination often triggers compensatory mechanisms (*Teng et al., 2013; Rossi et al., 2015; Vu et al., 2015; Ma et al., 2019; El-Brolosy et al., 2019*).

Our study uncovers a previously unrecognized connection between circadian clock genes and proteasome function. While previous work demonstrated that the circadian clock rhythmically regulates proteasome components in *Drosophila* fat bodies under

281 dietary restriction (*Hwangbo et al., 2023*), we now show that *Mettl5* modulates clock
282 protein synthesis and degradation in clock neurons by influencing proteasome activity.
283 This regulation likely occurs through *Mettl5*-mediated ribosomal methylation in clock
284 neurons, which impacts the proteasome degradation pathway (*Costa et al., 2019*),
285 ultimately altering clock protein dynamics.

286 Mettl5 represents a novel integrator of rRNA methylation and proteasome function, providing a
287 mechanism to balance protein synthesis and degradation. Interestingly, we observed specific effects
288 on both transcriptional and translational outputs, with particular proteasome subunits showing
289 differential regulation. This specificity may arise from either selective translational control by Mettl5
290 or additional layers of regulation through protein-protein interactions. These findings suggest an
291 intricate regulatory network coordinating these processes, though further studies are needed to
292 elucidate the underlying mechanisms.

293 Our results reveal complex relationships between clock genes and sleep regulation. While *cyc* loss-
294 of-function alleles show enhanced sleep rebound in females (*Shaw et al., 2002*), *Mettl5*^{1bp} mutants
295 with elevated PER protein exhibit reduced rebound. Notably, *Mettl5*'s regulatory effects display tissue
296 specificity - although absent in canonical clock neurons, *Mettl5*-Gal4 is expressed in distinct neurons
297 and glia that appear crucial for sleep regulation. This expression pattern, combined with Clock's
298 broader distribution (*Patop et al., 2023*), suggests specialized circuits for sleep homeostasis that
299 warrant further investigation.

300 Evidence indicates that sleep functions in development, metabolism and neuronal plasticity (*Anafi*
301 *et al., 2019*). Sleep exerts effects on neuronal plasticity by modifying synapses. The synaptic
302 homeostasis theory proposes that sleep has a role in downscale synaptic strength (*Tononi and Cirelli,*
303 *2006*). Indeed, synapse markers progressively decrease during sleep in both mammals and *Drosophila*
304 brains (*López-Varea et al., 2021; Vyazovskiy et al., 2008; Gilestro et al., 2009; Liu et al., 2010*) More
305 importantly, evidence indicates that sleep need and protein levels in synapse are tightly linked. Studies
306 of the presynaptic active zone have shown that synaptic plasticity regulates sleep homeostasis (*Huang*
307 *et al., 2020*). Genome-wide proteomic studies of synapse in mouse brain indicate that the synaptic
308 proteins peak around dusk and dawn (*Noya et al., 2019; Brüning et al., 2019*). Sleep deprivation

experiments have demonstrated that the sleep drive is significantly dependent on the cycling of proteins and phosphoproteins in synapses, in contrast to mRNAs (*Noya et al., 2019; Brüning et al., 2019*). These results suggest that the gene expression regulation at the protein level is crucial for sleep. Consistently, we detected changes in the quantity of axons in *Mettl5*^{1bp}, suggesting a possible regulation of neural circuits by *Mettl5*.

The mechanism by which METTL5 regulates translation warrants further investigation. Previous studies have demonstrated that METTL5 influences translation (Rong et al., 2020; Peng et al., 2022), but whether the mechanisms identified here are conserved across other systems remains an intriguing question. In our analysis, we observed increased usage of aspartate (Asp) codons in *Mettl5* mutants. Notably, prior work has linked codon usage to PER protein function—specifically, a codon-optimized version of PER failed to rescue circadian rhythmicity in *per* mutant flies, unlike the wild-type version (Fu et al., 2016). Further analysis revealed that PER protein levels were elevated in these mutants, suggesting that codon optimization enhances PER expression (Figure 2B in Fu et al., 2016). Strikingly, when we examined the codon-optimized region from Fu et al. (2016), we found that GAC (Asp) was highly enriched, raising the possibility that *Mettl5* mutation affects PER protein accumulation by altering GAC codon usage. Additional experiments will be needed to validate this hypothesis. Furthermore, we detected changes in upstream open reading frames (uORFs) in *Mettl5* mutants, but their relationship to translational regulation requires further exploration.

Our study demonstrates that ribosomal components can exert gene-specific regulatory functions, building upon previous work showing context-dependent ribosome specialization (*Simsek et al., 2017*). In *Mettl5* mutants, we observed distinct alterations in the translational efficiency of specific genes. These effects could potentially arise through two non-exclusive mechanisms: (1) *Mettl5*-mediated rRNA modifications may modulate ribosomal binding affinity for particular mRNA sequences, or (2) these modifications might contribute to the formation of specialized ribosome populations that preferentially translate specific subsets of mRNAs. Future studies will be required to distinguish between these possibilities and fully elucidate the underlying molecular mechanisms.

Material and methods

Drosophila Strains

Fly stocks used in this study were maintained under standard culture conditions. We used the w^{1118} as the control strain. The following flies were obtained from Bloomington Stock Center: w^{1118} (Bl: 5905), *Mettl5*-Gal4 (Bl: 19514), *Repo*-Gal4 (Bl: 7415), *nSyb*-Gal4 (Bl: 51941), *pdf*-Gal4 (Bl: 41286), Clk^{JRK} (Bl: 80927), per^{01}(Bl: 80917), $Fmr1^{\Delta 50M}$(Bl: 6930)，UAS-*Trmt112*RNAi (VDRC: 101515), UAS-DenMark,UAS-*syt*.eGFP (Bl: 33064), UAS-GFPstinger (from Yi Rao's lab), UAS-*Fmr1* (Bl: 6931), UAS-*Mettl5* (FlyORF: F000760) are from Fly ORF collection. UAS-*Mettl5m*-3HA (generated in this study).

$Mettl5^{1bp}$ and $Mettl5^{9bp}$ mutants were generated by the CRISPR/Cas system as described previously (*Cheng et al., 2020*). The target gRNA was designed with an online tool: http://tools.flycrispr.molbio.wisc.edu/targetFinder/. A target sequence was chosen that has the sequence of 5'- GAGTGGGGTACTGTTCCAAC**AGG** with the PAM sequence in bold. Mutations were verified by genomic PCR and sequencing.

Sleep behavior assays

All sleep assays were conducted in a controlled environment incubator maintained at 25 ± 1°C with 60% ± 5% relative humidity. We maintained a 12:12 light-dark cycle with lights on at ZT0 (06:30) and off at ZT12 (18:30). Fly activity was monitored using the Drosophila Activity Monitoring System (Trikinetics, Waltham, MA). Following a 2-day acclimation period, we recorded locomotor activity at 1-minute intervals for 3 consecutive days. Data analysis was performed using pysolo (*Gilestro and Cirelli, 2009*), with sleep defined as ≥5 minutes of continuous inactivity.

Mechanical sleep deprivation was performed using the SNAP method to keep flies awake for 12 h overnight (*Shaw et al., 2002*). Sleep deprivation is applied by mechanical stimuli using a timer-controlled rotating shaker. The intensity of stimuli was 1500 rpm once every minute (2 s/1 min) (*Shimizu et al., 2008*). Baseline sleep was established from 24-hour recordings prior to deprivation. Sleep loss and recovery were quantified according to previous publication (Cirelli C et al., 2005).

Regarding the 'awake %' metric, it indicates that at specific time points (e.g., ZT14), the percentage of awake fruit fly population at that moment. At ZT19, we evaluated arousal thresholds by administering a standardized gentle mechanical stimulus. Responsiveness was determined by monitoring activity for 1 minutes post-stimulation. Flies showing no activity during this window were

365 scored as non-responsive. We calculated arousal percentages from the proportion of flies that
366 awakened in response to stimulation.

367 Circadian rhythm of individual male flies was measured using the Drosophila Activity Monitoring
368 (DAM) System (Trikinetics). Male flies were loaded individually into glass tubes with a length of
369 65 mm and an inner diameter of 5 mm. The tubes contained standard cornmeal fly food at one end and
370 were sealed with a cotton stopper at the other end. The flies were entrained to a 12 h light/12 h dark
371 cycle for 3 days and then released to constant darkness for at least six days to measure their
372 rhythmicity.Data analysis is done on a Macintosh computer running the FaasX (Fly activity analysis
373 suite) software.

374 **Statistical analysis**

375 All statistical analyses were performed using GraphPad Prism 5 software. For sleep parameter
376 comparisons, we used nonparametric tests including the two-tailed Mann-Whitney test for pairwise
377 comparisons and one-way ANOVA with Tukey's post hoc test for multiple comparisons. qPCR data
378 were analyzed using unpaired Student's t-tests, while lifespan data were evaluated with Log-rank
379 (Mantel-Cox) tests. The specific statistical test used for each experiment is indicated in the
380 corresponding figure. In all analyses, a p-value of less than 0.05 was considered statistically significant.

381 **Quantitative PCR**

382 Total RNA was extracted from cells and tissues using the TRNzol Universal Reagent (Tiangen #DP4-
383 02). For cDNA synthesis, we employed the PrimeScript RT reagent Kit with gDNA Eraser (TAKARA
384 #RR047A) following the manufacturer's protocol. Quantitative PCR was carried out using SuperReal
385 PreMix Plus (SYBR Green) (Tiangen #DP4-02). *RP49* served as the endogenous reference gene for
386 normalization across samples. All experiments included three independent biological replicates to
387 ensure reproducibility. The primers used in this experiment are *RP49*-F:
388 CGGTTACGGATCGAACAAGC; *RP49*-R: CTTGCGCTTCTTGGAGGAGA; *Mettl5*-F:
389 CGGTTTCTGGAGGTGGC; *Mettl5*-R: GCTGGCGTCGATGTTGTAC..

390 **Imaging and analysis of axon volume**

391 We quantified small LNvs axon volume using ImageJ's Object Counter 3D plugin to measure pixel
392 counts from raw images. Image processing involved applying a standardized threshold that clearly

visualized intact axons in control samples. For consistent measurements, we specifically analyzed the axon span between the first axonal bifurcation and the terminal tip, as indicated by the white rectangular markers in Figure 8.

Sample collection and library construction for Ribo-seq and RNAseq

For sample collection, w^{1118} and *Mettl5*^{1bp} *Drosophila* were harvested at ZT15, immediately transferred to centrifuge tubes, and flash-frozen in liquid nitrogen. Fly heads were subsequently separated and collected while frozen, with three biological replicates prepared for each genotype. Each sample was equally divided for parallel RNA-seq and Ribo-seq analyses. For Ribo-seq library preparation, samples were lysed in buffer containing 50 mg/mL cycloheximide (Novogen, China) to preserve ribosome positioning, followed by RNase I digestion to generate ribosome-protected fragments (RPFs). Monosomes were isolated using MicroSpin S-400 HR size-exclusion chromatography, followed by rRNA depletion and PAGE purification to select 20-38 nt RPFs. Purified fragments underwent end repair, adapter ligation, reverse transcription, and PCR amplification before Illumina PE150 sequencing. For RNA-seq, total RNA was extracted using TRIzol reagent, with cDNA libraries prepared and sequenced using Illumina PE150 by Novogen. Raw sequencing data in FASTQ format were processed to remove adapter sequences, reads containing N bases, and low-quality reads, while simultaneously calculating Q20/Q30 scores and GC content to generate clean reads for downstream analysis.

RNA-seq analysis

We performed genome alignment and transcriptome analysis using the following pipeline: First, we built a Hisat2 index (v2.0.5) for the Drosophila melanogaster reference genome (dm6 assembly). Clean paired-end reads were then aligned to this reference using Hisat2 (v2.0.5) (*Kim et al., 2019*). The resulting alignments were processed using StringTie (v1.3.3b) (*Pertea et al., 2015*) for reference-based transcript assembly. For gene-level quantification, we used FeatureCounts (v1.5.0) (*Liao et al., 2014*) to count reads mapped to each annotated gene. Differential expression analysis between w^{1118} and *Mettl5*^{1bp} was conducted with DESeq2 (v1.20.0) (*Pertea et al., 2015*), with genes meeting both criteria (adjusted p-value < 0.05 and absolute log2 fold change ≥ 1) considered statistically significant.

Ribo-seq analysis

We implemented a comprehensive Ribo-seq analysis pipeline beginning with quality filtering using Bowtie (*Liao et al., 2014*) to remove reads aligning to non-coding RNAs (rRNA, tRNA, snoRNA, snRNA from FlyBase Release 6.13) with a 2-mismatch allowance (-v 2). The remaining ribosome-protected fragments (RPFs) were mapped to the *Drosophila melanogaster* genome (FlyBase Release 6.13) using STAR (v2.7.3a) (Dobin et al., 2013), followed by transcript-level alignment to protein-coding sequences using Bowtie (v1.2.2) (*Langmead et al., 2009*) with parameters "-a -v 2". CDS-aligned RPFs were quantified using featureCounts (Subread v1.6.3) and normalized as RPKM. Differential expression analysis was performed with DESeq2 (v1.14.1) (*Love et al., 2014*) using thresholds of $|\log2FC| \geq 0.265$ and $padj < 0.05$, while translation efficiency differences were assessed using RiboDiff. Data quality was verified through riboWaltz (v1.1.0) (*Lauria et al., 2018*) for 3-nt periodicity and reading frame analysis, with Ribocode (*Xiao et al., 2018*) employed for P-site positioning and uORF motif analysis. Functional enrichment analyses (GO, KEGG, GSEA) were conducted using clusterProfiler (v4.5.2.002) (Wu et al., 2021), with results visualized through ggplot2-generated plots and GO term simplification performed using SimplifyEnrichment (*Gu and Hübschmann, 2022*).

Immunofluorescence experiments

We performed immunofluorescence staining on 7-15 days old adult flies (unless otherwise specified). Flies were anesthetized with CO_2 and dissected in ice-cold 0.03% PBST (1× PBS with 0.03% Triton X-100; Sigma, T9284). Samples were fixed in 2% paraformaldehyde (PFA) for 55 minutes at room temperature (RT), followed by four 15-minute washes in 0.03% PBST at RT. After blocking overnight at 4°C in 10% Normal Goat Serum (NGS; in 1× PBS with 2% Triton), samples were incubated with primary antibodies for 24 hours at 4°C. Primary antibodies included rat anti-Elav (DSHB, 9F8A9; 1:200) and mouse anti-Repo (DSHB, 8D12; 1:200), diluted in antibody buffer (1.25% PBST, 1% NGS). Following four 15-minute washes in 1× PBS with 1% Triton at RT, samples were incubated overnight at 4°C with secondary antibodies: Alexa Fluor™ 568 (Thermo Fisher, A11004; 1:200) and Alexa Fluor™ 647 (Thermo Fisher, A21247; 1:200). After four additional 15-minute washes in 1× PBS with 1% Triton at RT, samples were mounted using DAPI-containing antifade mounting medium (Solarbio, S2110).

Images were acquired using a Leica SP8 confocal microscope with LAS X software, applying auto Z-brightness correction when needed for signal uniformity. Images were processed in Adobe Photoshop CS6 and figures assembled in Adobe Illustrator 2020. PDF immunofluorescence followed the same protocol. All experiments included ≥3 biological replicates, each containing ≥10 flies. Fluorescence intensity was quantified using ImageJ.

Western Blotting

Protein samples were prepared by homogenizing approximately 30 fly heads in RIPA lysis buffer (150 mM NaCl, 1.0% NP-40, 0.5% sodium deoxycholate, 0.1% SDS, 50 mM Tris-HCl, pH 8.0) supplemented with protease (CW2200S) and phosphatase (CW2383S) inhibitor cocktails according to manufacturer specifications. Lysates were mixed with 2× SDS loading buffer, boiled at 100°C for 5 min, and immediately cooled on ice.

For immunoblotting, membranes were probed with rabbit anti-PER primary antibody (1:5000 dilution; kindly provided by Dr. Jeffrey Price's laboratory, University of Missouri-Kansas City) overnight at 4°C, followed by incubation with HRP-conjugated goat anti-rabbit IgG secondary antibody (1:1500; ABclonal, AS014) for 4 hr at room temperature. Protein signals were detected using ECL substrate (ABclonal, RM00021P) and imaged with an Amersham ImageQuant 800 system (GE Healthcare). Band intensities were quantified using ImageJ software, with three biological replicates performed for statistical reliability.

LC-MS/MS analysis of m^6A levels

Total RNA was isolated from cells and tissues using TRNzol Universal Reagent (Tiangen, #DP4-02). For 18S rRNA purification, we separated total RNA by polyacrylamide gel electrophoresis followed by gel extraction. Our analysis utilized ribonucleoside standards including adenosine (rA) and N6-methyladenosine (N6 mA), with a mobile phase consisting of methanol:ddH2O (v/v).

For each biological replicate, 1 μg of total RNA or purified 18S rRNA was digested to single nucleosides using Nucleoside Digestion Mix (NEB, #M0649). Proteins were precipitated by adding a 4:1 methanol:digest ratio and incubating at -20°C for 2 hours. Quantitative analysis was performed using multiple reaction monitoring (MRM) with the following transitions: 268.10275→136.0621 (rA), 282.11835→150.0774 (N6 mA).

Negative geotaxis RING assay

Climbing assays were performed following a 12-hour recovery period after CO2 anesthesia, using 200 flies per genotype distributed across 10 vials (20 flies/vial) marked at 90 mm height. Each assay consisted of three trials separated by 15-minute intervals, initiated by sharply tapping vials three times to induce negative geotaxis, with the number of flies reaching the 90 mm mark within 10 seconds recorded per trial. Five groups were tested per genotype (15 trials total). All assays were video recorded under standardized conditions with the camera positioned 20 cm from vials and uniform backlighting provided by a white open-faced box to ensure consistent imaging quality.

Data availability

The RNA-seq and Ribo-seq data from this publication have been deposited to the NCBI bioproject database https://www.ncbi.nlm.nih.gov/bioproject/ and assigned the identifier PRJNA994860.

Acknowledgements

This work was supported by National Natural Science Foundation of China (Grant No. 32070492 and 32122017) to Juan Du. We would also like to acknowledge the 2115 Talent Development Program of China Agricultural University.

Author contributions

XY, XW and TF designed and performed the experiments, analyzed the data and wrote the manuscript. XY performed the bioinformatics analysis, analyzed the data and edited the manuscript. YR analyzed data and edited the manuscript. JD designed experiments, analyzed data, wrote and edited the manuscript. All authors have read and approved the final manuscript.

Declaration of interest

The authors declare that they have no conflict of interest.

Supplementary information

Supplementary Figures S1-S11

502 **Figure legends**

503 **Figure 1 *Mettl5* is a regulator of *Drosophila* sleep.**

504 (A) Diagram illustrating CRISPR-Cas knockout of 1 or 9 bases in the *Mettl5* gene. (B) Relative
505 expression of *Mettl5* mRNA in homozygous *Mettl5*^{1bp} and *Mettl5*^{9bp} mutant male flies compared to
506 control flies. (C) Sleep curve throughout the day for *Mettl5* mutant male flies (blue) and control flies
507 (black). (D) Total sleep of *Mettl5* mutant male flies and control flies in 24 hours. (E) Total sleep of
508 *Mettl5* mutant male flies and control flies within day and night, respectively. (F) Sleep bout duration
509 of *Mettl5* mutant male flies and control flies. (G) Number of sleep bouts of *Mettl5* mutant male flies
510 and control flies. (H) Percentage of awake for *Mettl5* mutant flies and control flies. (I) Sleep curve is
511 tracked throughout the entire day prior to sleep deprivation and during the daytime sleep rebound
512 period. (J) *Mettl5* mRNA expression level at different time points. W(wake), SD (sleep deprivation),
513 SR (sleep recovery). (K) Sleep curve is tracked throughout the entire day prior to sleep deprivation
514 and during the daytime sleep rebound period in *Mettl5* mutant male flies (blue) and control flies (black).
515 (L) Response to sleep deprivation and performance measures in *Mettl5* mutants and controls. Black
516 bars represent the amount of sleep lost during the 24-hour sleep deprivation period, blue bars indicate
517 the amount of sleep regained, whereas the red bars indicate the proportion of sleep recovered (right y-
518 axis). (M) Sleep arousal of *Mettl5*^{1bp} male flies and control flies at ZT19. (N) Sleep curve throughout
519 the day for the following genotypes: *w*^{1118}(black), *Mettl5*^{1bp}/+ (blue)*, and Mettl5-Gal4, UAS-Mettl5,*
520 *Mettl5*^{1bp}/+(pink). (O) Total sleep of the indicated genotypes. (P) Sleep bout duration of the indicated
521 genotypes. (Q) Number of sleep bouts of the indicated genotypes. (R) Percentage of awake for the
522 indicated genotypes. For * stands for $p<0.05$, ** stands for $p<0.01$, *** stands for $p<0.001$, *ns* stands
523 for not significant. For letter-based annotations, Groups with no significant differences share the same
524 letter, Groups with significant differences are assigned new letters.

525 **Figure 2 *Mettl5* regulation of *Drosophila* sleep was dependent on its methyltransferase activity.**

526 (A) The m^{6}A level in the total RNA of *Mettl5* mutant male flies. (B) The m^{6}A level in the 18S rRNA
527 of *Mettl5* mutant male flies. (C) The sleep curve throughout the day shows the sleep pattern of induced
528 *Trmt112* RNAi male flies and control flies. (D) Total sleep of induced *Trmt112* RNAi male flies and
529 control flies. (E) Sleep bout duration in induced *Trmt112* RNAi male flies and control flies. (F)

Number of sleep bouts in induced *Trmt112* RNAi male flies and control flies. (G) Percentage of awake in *Trmt112* RNAi and control flies. (H) Sleep curve throughout the day for *Mettl5* mutant male flies, induced *Mettl5m* over expression male flies and control flies. (I) Total sleep of *Mettl5* mutant male flies, induced *Mettl5m* over expression male flies and control flies. (J) Sleep bout duration in *Mettl5* mutant male flies, induced *Mettl5* over expression male flies and control flies. (K) Number of sleep bouts in *Mettl5* mutant male flies, induced *Mettl5* over expression male flies and control flies. (L) Percentage of awake in *Mettl5* mutant male flies, induced *Mettl5* over expression male flies and control flies. For * stands for $p<0.05$, ** stands for $p<0.01$, *** stands for $p<0.001$, *ns* stands for not significant. For letter-based annotations, Groups with no significant differences share the same letter, Groups with significant differences are assigned new letters.

Figure 3 RNA-seq and Ribo-seq analysis revealed changes in the gene profile of *Mettl5^{1bp}*.

(A) Venn diagram depicting the number of significant differentially expressed genes revealed by RNA-seq and Ribo-seq. (B) Volcano plot representing the differentially expressed genes identified by RNA-seq. Genes that met the criteria of $|\log2(\text{fold-change})| \geq 1$ and p.adjust < 0.05 were considered significantly expressed, marked in orange for downregulation and green for upregulation, comparing with the controls. (C) Volcano plot representing the differentially expressed genes identified by Ribo-seq. Candidates that satisfied the criteria of $|\log_2(\text{fold-change})| \geq 0.265$ and p.adjust <0.05 were regarded as significantly expressed, marked in red for downregulation and blue for upregulation, respectively. (D-K) Gene set enrichment analysis of differentially expressed genes revealed by RNA-seq (D-G) and Ribo-seq (H-K). All the plots are generated using the KEGG gene set database. The bar chart at the bottom of each panel shows the distribution of target genes for each pathway according to their rank position. Each vertical line represents a gene. Genes on the left show positive correlation with *Mettl5^{1bp}*, while, genes on the right show negative correlation with *Mettl5^{1bp}*. The green line indicates the enrichment score (ES), and NES stands for normalized enrichment score. (L) Distribution of the differentially expressed genes revealed by both RNA-seq and Ribo-seq. (M) Cumulative distribution of TE frequencies among *w^{1118}* and *Mettl5^{1bp}* (N, O) GO and KEGG enrichment of significantly changed TE-related genes between *w^{1118}* and *Mettl5^{1bp}*. The color of the bar indicates the enrichment p.adjust value. (P) KEGG network showing the top 10 pathway and

associated genes. The size of the dots represents the number of genes in the pathway.

Figure 4. Clock genes expression mediated the sleep phenotype caused by *Mettl5* mutation.

(A-C) Fold changes in clock genes with significant expression level differences between w^{1118} and $Mettl5^{1bp}$ were observed in RNA-seq, Ribo-seq, and translation efficiency analyses. (D) The gene expression levels of per at 4 different timepoints of w^{1118} and $Mettl5^{1bp}$. (E) Western blot analysis of PER protein and Tubulin protein at 4 different timepoints, (F) along with their ratio quantification. (G) Representative image of PER protein immunofluorescence staining in the small ventral lateral neurons (small LNvs). (H) Statistical analysis of the immunofluorescence intensity for PER in small LNvs. (I) Sleep curve throughout the day for $Mettl5^{1bp}$, per^{01}, double mutant and control flies. (J) Total sleep for $Mettl5^{1bp}$, per^{01}, double mutant and control flies. (K) Percentage of awake time in $Mettl5^{1bp}$ flies, partially rescued by double mutant flies. (L) Sleep curve throughout the day for $Mettl5^{1bp}$, per^{01}, double mutant and control flies. (M) Total sleep for $Mettl5^{1bp}$, per^{01}, double mutant and control flies. (N) Percentage of awake time in $Mettl5^{1bp}$ flies, partially rescued by double mutant flies. (O) Fold changes in proteasome subunits with significant expression level differences between w^{1118} and $Mettl5^{1bp}$ were observed in RNA-seq, Ribo-seq, and translation efficiency analyses. For statistical significance, * stands for $p<0.05$, ** stands for $p<0.01$, *** stands for $p<0.001$, *ns* stands for not significant.

Figure 5 A working model illustrating the role of *Mettl5* in *Drosophila* sleep was presented.

Figure 6 The axon complexity was found to be affected by $Mettl5^{1bp}$

(A–C) Representative confocal micrographs of small ventral lateral neuron (s-LNv) axonal terminals across different genotypes. Presynaptic structures were visualized using *syt*-eGFP (green), which colocalizes with endogenous synaptic vesicles: (A) control (B) Fmr1 overexpression and (C) Fmr1 null mutant. (D) Quantification of s-LNv axonal terminal volumes corresponding to genotypes in (A–C). (E–H) Representative images of axonal terminal morphology in control flies at four time points: ZT0, ZT6, ZT12, and ZT18. (I–L) Representative images of axonal terminal morphology in *Mettl5* mutant flies at ZT0, ZT6, ZT12, and ZT18. (M) Quantitative comparison of axonal terminal volumes between control and Mettl5 mutant flies at different time points. Scale bar: 50 μm. For statistical significance, * stands for $p<0.05$, ** stands for $p<0.01$, *** stands for $p<0.001$, *ns* stands for not significant.

586 **Table 1 Circadian rhythm phenotypes of various mutants.**

587

588 **References**

589 Anafi RC, Kayser MS, Raizen DM. 2019. Exploring phylogeny to find the function of sleep. *Nature*
590 *Reviews Neuroscience* 20: 109-116.

591 Brüning F, Noya SB, Bange T, Koutsouli S, Rudolph JD, Tyagarajan SK, Cox J, Mann M, Brown SA,
592 and Robles MS. 2019. Sleep-wake cycles drive daily dynamics of synaptic
593 phosphorylation. *Science* 366: eaav3617.

594 Bushey D, Tononi G, Cirelli C. 2011. Sleep and synaptic homeostasis: structural evidence in *Drosophila*.
595 *Science* 332: 1576-1581.

596 Cheng L, Zhang Y, Zhang Y, Chen T, Xu YZ, Rong YS. 2020. Loss of the RNA trimethylguanosine cap
597 is compatible with nuclear accumulation of spliceosomal snRNAs but not pre-mRNA splicing or
598 snRNA processing during animal development. *PLoS Genetics* 16: e1009098.

599 Chiu JC , Vanselow JT, Kramer A, Edery I. 2008. The phosphooccupancy of an atypical SLIMB-binding
600 site on PERIOD that is phosphorylated by DOUBLETIME controls the pace of the clock. *Genes Dev*.
601 22, 1758–1772.

602 Cirelli C, Bushey D, Hill S, Huber R, Kreber R, Ganetzky B, Tononi G. 2005. Reduced sleep in
603 Drosophila Shaker mutants. Nature 434:1087-92.

604 Costa RO, Martins H, Martins LF, Cwetsch AW, Mele M, Pedro JR, Tomé D, Jeon NL, Cancedda L,
605 Jaffrey SR, Almeida RD. 2019. Synaptogenesis stimulates a proteasome-mediated ribosome
606 reduction in axons. *Cell Reports* 28: 864-876.

607 Desvergne A, Ugarte N, Radjei S, Gareil M, Petropoulos I, Friguet B. 2016. Circadian modulation of
608 proteasome activity and accumulation of oxidized protein in human embryonic kidney HEK 293 cells
609 and primary dermal fibroblasts. *Free Radical Biology and Medicine* 94: 195-207.

610 Dobin A, Davis CA, Schlesinger F, Drenkow J, Zaleski C, Jha S, Batut P, Chaisson M, Gingeras, TR.
611 2013. STAR: ultrafast universal RNA-seq aligner. *Bioinformatics* 29: 15-21.

612 Du J, Lv P, Fu T, Wei Y, Zhao Z. 2021. Regulation of sleep in *Drosophila melanogaster*. *Advances in*
613 *Insect Physiology* 60: 119-168.

El-Brolosy MA, Kontarakis Z, Rossi A, Kuenne C, Gunther S, Fukuda N, Kikhi K, Boezio GLM, Takacs CM, Lai SL. 2019. Genetic compensation triggered by mutant mRNA degradation. *Nature* 568: 193-197.

Fernández-Cruz I, Sánchez-Díaz I, Narváez-Padilla V, Reynaud E. 2020. Rpt2 proteasome subunit reduction causes Parkinson's disease like symptoms in *Drosophila*. *IBRO Reports* 9: 65-77.

Fu J, Murphy KA, Zhou M, Li YH, Lam VH, Tabuloc CA, Chiu JC, Liu Y. 2016. Codon usage affects the structure and function of the *Drosophila* circadian clock protein PERIOD. *Genes & Development* 30:1761-75.

Galimberti V, Kinor N, Shav-Tal Y, Biggiogera M, Brüning A. 2016. The stress-inducible transcription factor ATF4 accumulates at specific rRNA-processing nucleolar regions after proteasome inhibition. *European Journal of Cell Biolog* 95: 389-400.

Gilestro GF, Tononi G, Cirelli C. 2009. Widespread changes in synaptic markers as a function of sleep and wakefulness in *Drosophila*. *Science* 324: 109-112.

Gilestro GF, Cirelli C. 2009. pySolo: a complete suite for sleep analysis in Drosophila. *Bioinformatics* 25: 1466-1467.

Grima B, Lamouroux A, Chélot E, Papin C, Limbourg-Bouchon B, Rouyer F. 2002. The F-box protein slimb controls the levels of clock proteins period and timeless. *Nature* 420:178-82.

Gu Z, Hübschmann D. 2022. simplifyEnrichment: A bioconductor package for clustering and visualizing functional enrichment results. *Genomics Proteomics Bioinformatics* 21: 190-202.

Huang S, Piao C, Beuschel CB, Götz T, Sigrist SJ. 2020. Presynaptic active zone plasticity encodes sleep need in Drosophila. *Current Biology* 30: 1077-1091.

Hwangbo DS, Kwon YJ, Iwanaszko M, Jiang P, Abbasi L, Wright N, Alli S, Hutchison AL, Dinner AR, Braun RI, Allada R. 2023. Dietary restriction impacts peripheral circadian clock output important for longevity in *Drosophila*. *eLife* 12: RP86191.

Iyer LM, Zhang D, Aravind L. 2016. Adenine methylation in eukaryotes: Apprehending the complex evolutionary history and functional potential of an epigenetic modification. Bioessays. 38:27-40.

Kapetanou M, Athanasopoulou S, Gonos ES. 2022. Transcriptional regulatory networks of the proteasome in mammalian systems. *IUBMB Life* 74: 41-52.

642 Kim D, Paggi JM, Park C, Bennett C, Salzberg SL. 2019. Graph-based genome alignment and
643 genotyping with HISAT2 and HISAT-genotype. *Nature Biotechnology* 37: 907-915.
644 Ko HW, Jiang J, Edery I. 2002. Role for Slimb in the degradation of Drosophila period protein
645 phosphorylated by doubletime. *Nature* 420: 673–678.
646 Langmead B, Trapnell C, Pop M, Salzberg SL. 2009. Ultrafast and memory-efficient alignment of short
647 DNA sequences to the human genome. *Genome Biology* 10: R25.
648 Lauria F, Tebaldi T, Bernabò P, Groen EJN, Gillingwater TH, Viero G. 2018. riboWaltz: Optimization
649 of ribosome P-site positioning in ribosome profiling data. *PLoS Computational Biology* 14: e1006169.
650 Leismann J, Spagnuolo M, Pradhan M, Wacheul L, Vu MA, Musheev M, Mier P, Andrade-Navarro MA,
651 Graille M, Niehrs C, Lafontaine DL, Roignant JY. 2020. The 18S ribosomal RNA m^6A
652 methyltransferase *Mettl5* is required for normal walking behavior in *Drosophila*. *EMBO Reports* 21:
653 e49443.
654 Liao Y, Smyth GK, Shi W. 2014. featureCounts: an efficient general purpose program for assigning
655 sequence reads to genomic features. *Bioinformatics* 30: 923-930.
656 Liu ZW, Faraguna U, Cirelli C, Tononi G, Gao XB. 2010. Direct evidence for wake-related increases
657 and sleep-related decreases in synaptic strength in rodent cortex. *Journal Of Neuroscience* 30: 8671-
658 8675.
659 López-Varea A, Vega-Cuesta P, Ruiz-Gómez A, Ostalé CM, Molnar C, Hevia CF, Martín M, Organista
660 MF, de Celis J, Culí J, Esteban N, de Celis JF. 2021. Genome-wide phenotypic RNAi screen in the
661 Drosophila wing: phenotypic description of functional classes. G3 (Bethesda). *11*, jkab349. DOI:
662 10.1093/g3journal/jkab349. PMID: 34599810
663 Love MI, Huber W, Anders S. 2014. Moderated estimation of fold change and dispersion for RNA-seq
664 data with DESeq2. *Genome Biology* 15: 550.
665 Lyons LC, Vanrobaeys Y, Abel T. 2023. Sleep and memory: The impact of sleep deprivation on
666 transcription, translational control, and protein synthesis in the brain. *Journal Of Neurochemistry*
667 166: 24-46.
668 Ma Z, Zhu P, Shi H, Guo L, Zhang Q, Chen Y, Chen S, Zhang Z, Peng J, Chen J. 2019. PTC-bearing
669 mRNA elicits a genetic compensation response via Upf3a and COMPASS components. *Nature* 568:

259-263.

Noya SB, Colameo D, Brüning F, Spinnler A, Mircsof D, Opitz L, Mann M, Tyagarajan SK, Robles MS, Brown SA. 2019. The forebrain synaptic transcriptome is organized by clocks but its proteome is driven by sleep. *Science* 366: eaav2642.

Palanca A, Casafont I, Berciano MT, Lafarga M. 2014. Reactive nucleolar and Cajal body responses to proteasome inhibition in sensory ganglion neurons. *Biochimica et Biophysica Acta* 1842: 848-859.

Patop IL, Anduaga AM, Bussi IL, Ceriani MF, Kadener S. 2023. Organismal landscape of clock cells and circadian gene expression in *Drosophila*. bioRxiv [Preprint]. 2023.05.23.542009.

Peng H, Chen B, Wei W, Guo S, Han H, Yang C, Ma J, Wang L, Peng S, Kuang M, Lin S. 2022. N^6-methyladenosine (m^6A) in 18S rRNA promotes fatty acid metabolism and oncogenic transformation. *Nature Metabolism* 4:1041-54.

Pertea M, Pertea GM, Antonescu CM, Chang TC, Mendell JT, Salzberg SL. 2015. StringTie enables improved reconstruction of a transcriptome from RNA-seq reads. *Nature Biotechnology* 33: 290-295.

Philpott JM, Freeberg AM, Park J, Lee K, Ricci CG, Hunt SR, Narasimamurthy R, Segal DH, Robles R, Cai Y, Tripathi S, McCammon JA, Virshup DM, Chiu JC, Lee C, Partch CL. 2023. PERIOD phosphorylation leads to feedback inhibition of CK1 activity to control circadian period. *Molecular Cell* 83: 1677-1692.

Richard EM, Polla DL, Assir MZ, Contreras M, Shahzad M, Khan AA, Razzaq A, Akram J, Tarar MN, Blanpied TA, Ahmed ZM, Abou Jamra R, Wieczorek D, van Bokhoven H, Riazuddin S, Riazuddin S. 2019. Bi-allelic variants in METTL5 cause autosomal-recessive intellectual disability and microcephaly. *American Journal Of Human Genetics* 105: 869-878.

Rong B, Zhang Q, Wan J, Xing S, Dai R, Li Y, Cai J, Xie J, Song Y, Chen J, Zhang L, Yan G, Zhang W, Gao H, Han JJ, Qu Q, Ma H, Tian Y, Lan F. 2020. Ribosome 18S m^6A methyltransferase *METTL5* promotes translation initiation and breast cancer cell growth. *Cell Reports* 33:108544.

Rossi A, Kontarakis Z, Gerri C, Nolte H, Holper S, Kruger M, Stainier DY. 2015. Genetic compensation induced by deleterious mutations but not gene knockdowns. *Nature* 524: 230-233

Sepich-Poore C, Zheng Z, Schmitt E, Wen K, Zhang ZS, Cui XL, Dai Q, Zhu AC, Zhang L, Sanchez Castillo A, Tan H, Peng J, Zhuang X, He C, Nachtergaele S. 2022. The METTL5-TRMT112 N6-

698 methyladenosine methyltransferase complex regulates mRNA translation via 18S rRNA methylation.
699 *Journal Of Biological Chemistry* 298: 101590.
700 Shaw PJ, Tononi G, Greenspan RJ, Robinson DF. 2002. Stress response genes protect against lethal
701 effects of sleep deprivation in *Drosophila*. *Nature* 417: 287-291.
702 Shimizu H, Shimoda M, Yamaguchi T, Seong KH, Okamura T, Ishii S. 2008. *Drosophila* ATF-2
703 regulates sleep and locomotor activity in pacemaker neurons. *Molecular And Cellular Biology* 28:
704 6278-6289.
705 Simsek D, Tiu GC, Flynn RA, Byeon GW, Leppek K, Xu AF, Chang HY, Barna M. 2017. The
706 mammalian Ribo-interactome reveals ribosome functional diversity and heterogeneity. *Cell* 169:
707 1051-1065.e18.
708 Sun J, Zhou H, Chen Z, Zhang H, Cao Y, Yao X, Chen X, Liu B, Gao Z, Shen Y, Qi L, Sun H. 2023.
709 Altered m6A RNA methylation governs denervation-induced muscle atrophy by regulating ubiquitin
710 proteasome pathway. *J Transl Med.* 21:845.
711 Teng X, Dayhoff-Brannigan M, Cheng WC, Gilbert CE, Sing CN, Diny NL, Wheelan SJ, Dunham MJ,
712 Boeke JD, Pineda FJ. 2013. Genome-wide consequences of deleting any single gene. *Molecular Cell*
713 52: 485-494.
714 Tononi G, Cirelli C. 2006. Sleep function and synaptic homeostasis. *Sleep Medicine Reviews* 10: 49-62.
715 van Tran N, Ernst FGM, Hawley BR, Zorbas C, Ulryck N, Hackert P, Bohnsack KE, Bohnsack MT,
716 Jaffrey SR, Graille M, Lafontaine DLJ. 2019. The human 18S rRNA m^6A methyltransferase METTL5
717 is stabilized by TRMT112. *Nucleic Acids Research* 47: 7719-7733.
718 Vu V, Verster AJ, Schertzberg M, Chuluunbaatar T, Spensley M, Pajkic D, Hart GT, Moffat J, Fraser
719 AG. 2015. Natural variation in gene expression modulates the severity of mutant phenotypes. *Cell*
720 162: 391-402
721 Vyazovskiy VV, Cirelli C, Pfister-Genskow M, Faraguna U, Tononi G. 2008. Molecular and
722 electrophysiological evidence for net synaptic potentiation in wake and depression in sleep. *Nature*
723 *Neuroscience* 11: 200-208.
724 Xiao Z, Huang R, Xing X, Chen Y, Deng H, Yang X. 2018. De novo annotation and characterization of
725 the translatome with ribosome profiling data. *Nucleic Acids Research* 46: e61.

726 Wang L, Liang Y, Lin R, Xiong Q, Yu P, Ma J, Cheng M, Han H, Wang X, Wang G, Liang F, Pei Z,
727 Chen D, Yuan Q, Jiang YZ, Lin S. Mettl5 mediated 18S rRNA N6-methyladenosine (m^6A)
728 modification controls stem cell fate determination and neural function. 2020. *Genes & Diseases* 9:
729 268-274.
730 Wu T, Hu E, Xu S, Chen M, Guo P, Dai Z, Feng T, Zhou L, Tang W, Zhan L, Fu X, Liu S, Bo X, Yu G.
731 2021. clusterProfiler 4.0: A universal enrichment tool for interpreting omics data. *Innovation*
732 (Camb) 2: 100141.
733 Zhang L, Hirano A, Hsu PK, Jones CR, Sakai N, Okuro M, McMahon T, Yamazaki M, Xu Y, Saigoh N,
734 Saigoh K, Lin ST, Kaasik K, Nishino S, Ptáček LJ, Fu YH. 2016. A *PERIOD3* variant causes a
735 circadian phenotype and is associated with a seasonal mood trait. *Proceedings of the National*
736 *Academy of Sciences* 113: E1536-44
737

Figure 1

Mettl5 allele verification

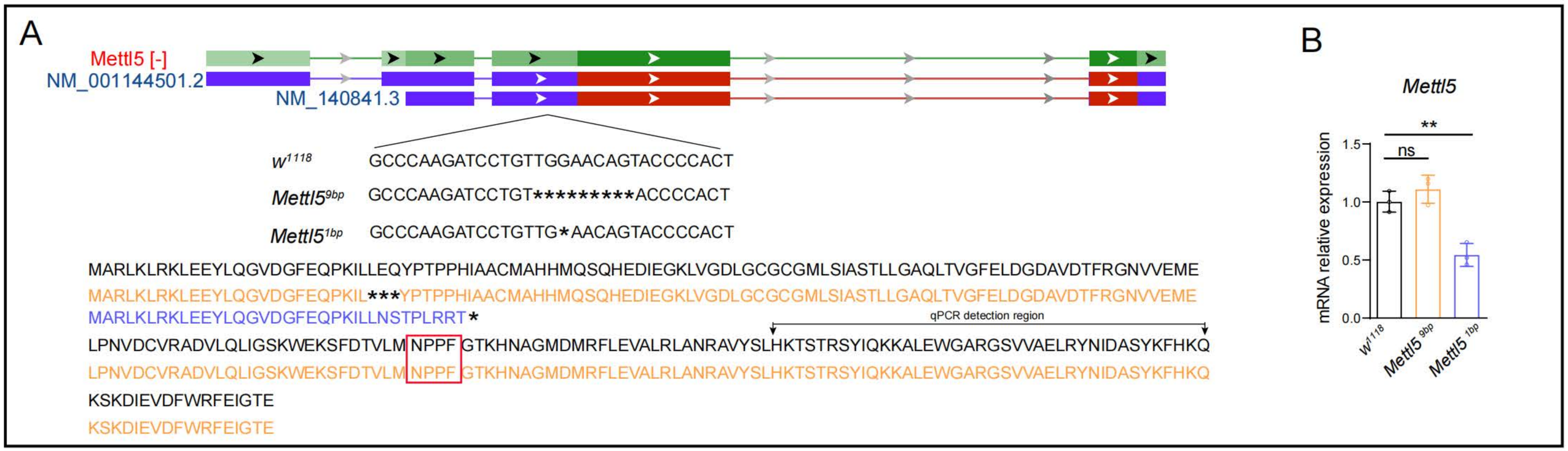

Sleep phenotypes

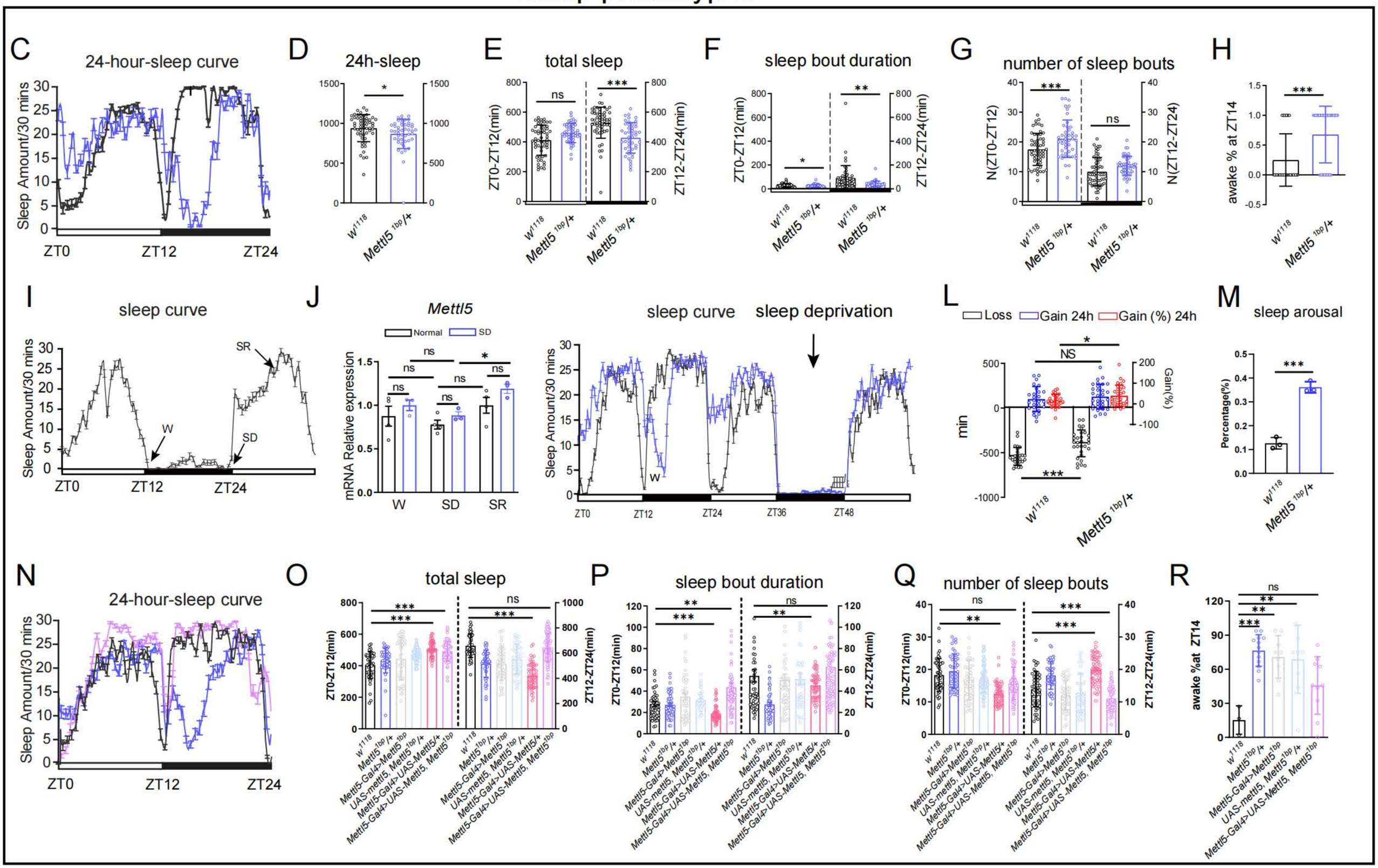

Figure 2

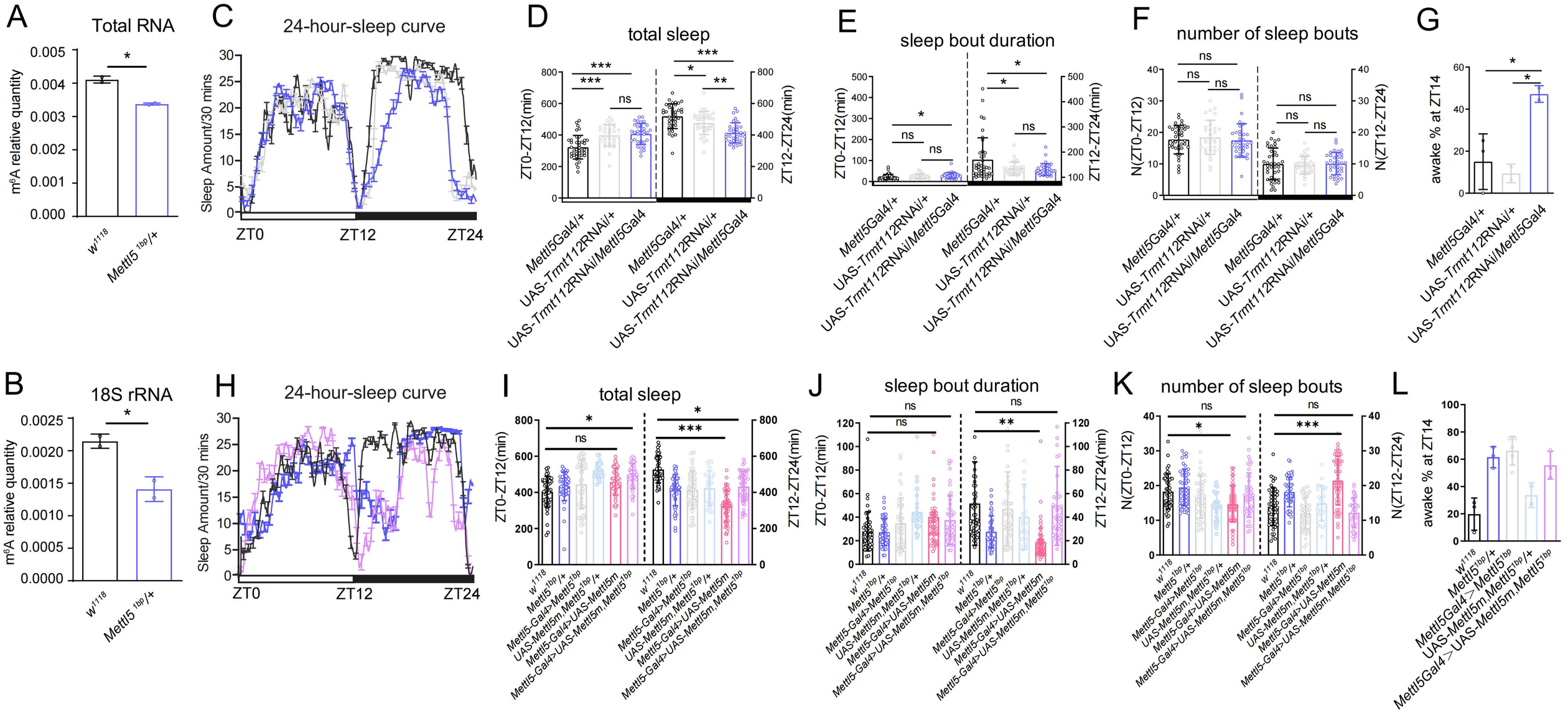
A
Total RNA
m6A relative quantity
0.005
0.004
0.003
0.002
0.001
0.000
*
w1118
Mettl5 1bp/+
C
24-hour-sleep curve
Sleep Amount/30 mins
ZT0
ZT12
ZT24
D
total sleep
ZT0-ZT12(min)
ZT12-ZT24(min)
***
***
ns
*
***
**
Mettl5Gal4/+
UAS-Trmt112RNAi/+
UAS-Trmt112RNAi/Mettl5Gal4
E
sleep bout duration
ZT0-ZT12(min)
ZT12-ZT24(min)
*
ns
ns
*
*
ns
F
number of sleep bouts
N(ZT0-ZT12)
N(ZT12-ZT24)
ns
ns
ns
ns
ns
ns
G
awake % at ZT14
*
*
B
18S rRNA
m6A relative quantity
0.0025
0.0020
0.0015
0.0010
0.0005
0.0000
*
w1118
Mettl5 1bp/+
H
24-hour-sleep curve
Sleep Amount/30 mins
ZT0
ZT12
ZT24
I
total sleep
ZT0-ZT12(min)
ZT12-ZT24(min)
*
ns
*
***
w1118
Mettl5 1bp/+
Mettl5-Gal4>Mettl5 1bp
UAS-Mettl5m,Mettl5 1bp/+
Mettl5-Gal4>UAS-Mettl5m
Mettl5-Gal4>UAS-Mettl5m,Mettl5 1bp
J
sleep bout duration
ZT0-ZT12(min)
ZT12-ZT24(min)
ns
ns
ns
**
K
number of sleep bouts
N(ZT0-ZT12)
N(ZT12-ZT24)
ns
*
ns
***
L
awake % at ZT14

Figure 3

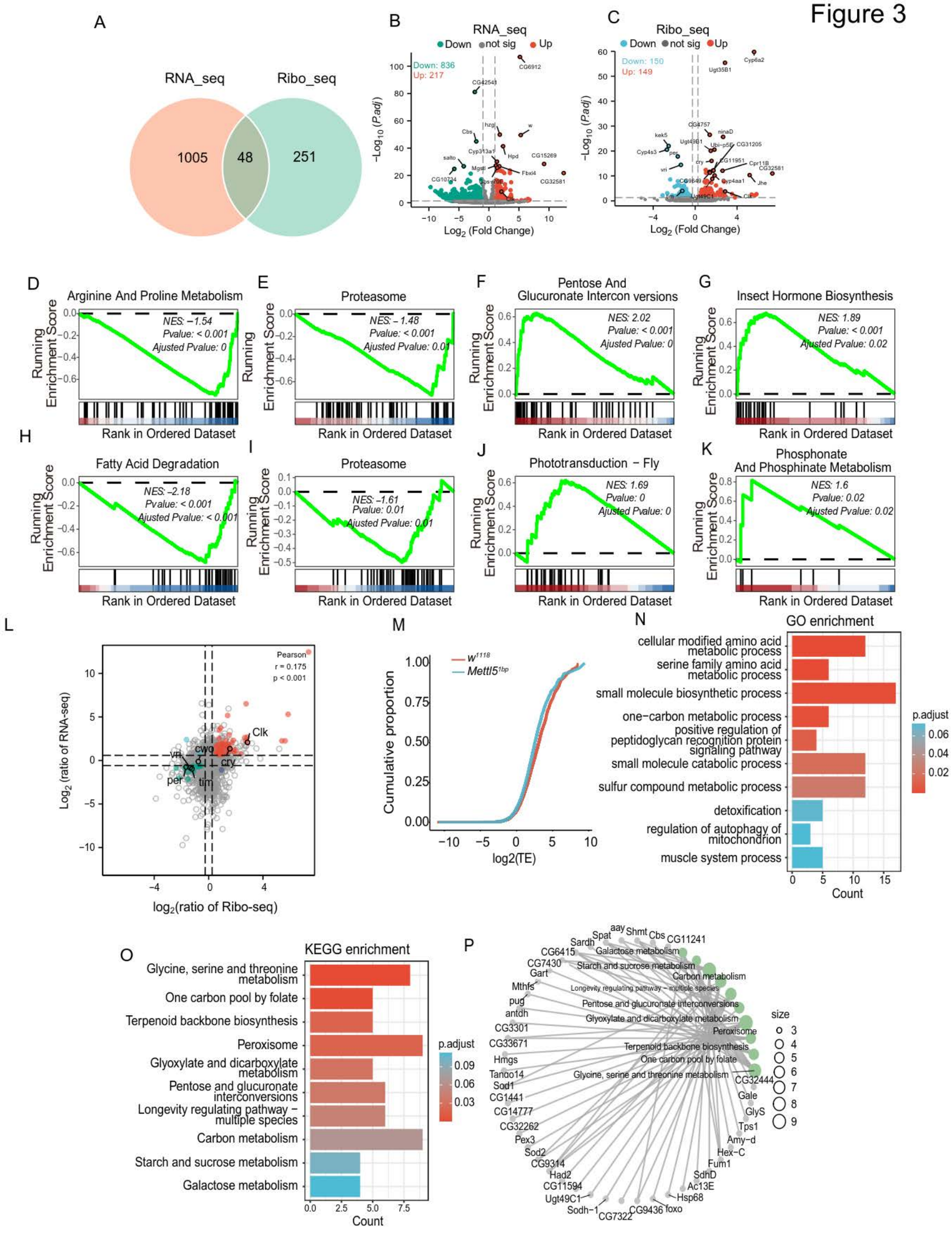
A
RNA_seq
Ribo_seq
1005
48
251
B
RNA_seq
Down
not sig
Up
Down: 836
Up: 217
CG6912
CG42541
hzg
w
Cbs
Cyp313a1
Hpd
CG15269
salto
Mgstl
Fbxl4
CG10734
CG32581
Clk
−Log10 (P.adj)
Log2 (Fold Change)
C
Ribo_seq
Down
not sig
Up
Down: 150
Up: 149
Cyp6a2
Ugt35B1
CG4757
ninaD
kek5
Ugt49B1
Ubi-p5E
CG31205
Cyp4s3
per
cry
CG11951
Cpr11B
CG32581
vri
CG9648
Cyp4aa1
Jhe
Clk
−Log10 (P.adj)
Log2 (Fold Change)
D
Arginine And Proline Metabolism
NES: −1.54
Pvalue: < 0.001
Ajusted Pvalue: 0
E
Proteasome
NES: − 1.48
Pvalue: < 0.001
Ajusted Pvalue: 0.01
F
Pentose And Glucuronate Intercon versions
NES: 2.02
Pvalue: < 0.001
Ajusted Pvalue: 0
G
Insect Hormone Biosynthesis
NES: 1.89
Pvalue: < 0.001
Ajusted Pvalue: 0.02
H
Fatty Acid Degradation
NES: −2.18
Pvalue: < 0.001
Ajusted Pvalue: < 0.001
I
Proteasome
NES: −1.61
Pvalue: 0.01
Ajusted Pvalue: 0.01
J
Phototransduction − Fly
NES: 1.69
Pvalue: 0
Ajusted Pvalue: 0
K
Phosphonate And Phosphinate Metabolism
NES: 1.6
Pvalue: 0.02
Ajusted Pvalue: 0.02
Running Enrichment Score
Rank in Ordered Dataset
L
Pearson
r = 0.175
p < 0.001
Clk
cwo
vri
cry
per
tim
Log2 (ratio of RNA-seq)
log2(ratio of Ribo-seq)
M
w1118
Mettl5 1bp
Cumulative proportion
log2(TE)
N
GO enrichment
cellular modified amino acid metabolic process
serine family amino acid metabolic process
small molecule biosynthetic process
one−carbon metabolic process
positive regulation of peptidoglycan recognition protein signaling pathway
small molecule catabolic process
sulfur compound metabolic process
detoxification
regulation of autophagy of mitochondrion
muscle system process
p.adjust
Count
O
KEGG enrichment
Glycine, serine and threonine metabolism
One carbon pool by folate
Terpenoid backbone biosynthesis
Peroxisome
Glyoxylate and dicarboxylate metabolism
Pentose and glucuronate interconversions
Longevity regulating pathway − multiple species
Carbon metabolism
Starch and sucrose metabolism
Galactose metabolism
p.adjust
Count
P
aay
Shmt
Cbs
CG11241
Spat
Sardh
CG6415
Galactose metabolism
CG7430
Starch and sucrose metabolism
Gart
Carbon metabolism
Mthfs
Longevity regulating pathway − multiple species
pug
Pentose and glucuronate interconversions
antdh
Glyoxylate and dicarboxylate metabolism
CG3301
Peroxisome
CG33671
Terpenoid backbone biosynthesis
Hmgs
One carbon pool by folate
Tango14
Glycine, serine and threonine metabolism
Sod1
CG32444
CG1441
Gale
CG14777
GlyS
CG32262
Tps1
Pex3
Amy-d
Sod2
Hex-C
CG9314
Fum1
Had2
SdhD
CG11594
Ac13E
Ugt49C1
Hsp68
Sodh-1
CG9436
foxo
CG7322
size

Figure 4

Differential expression of clock genes

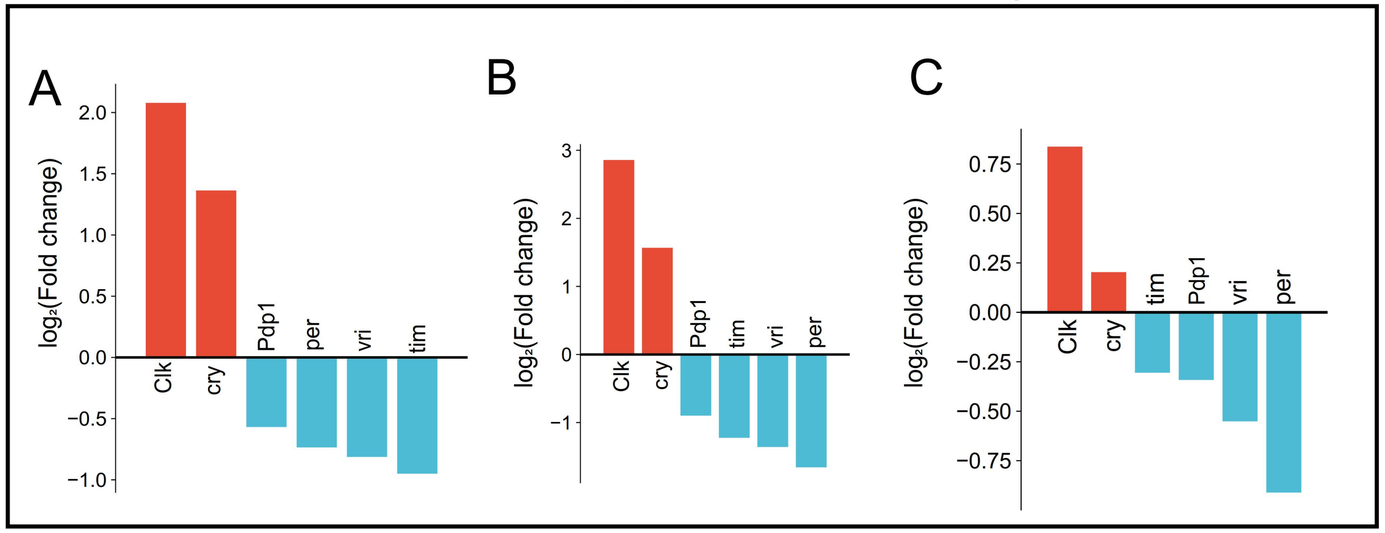

Differential expression of protesome genes

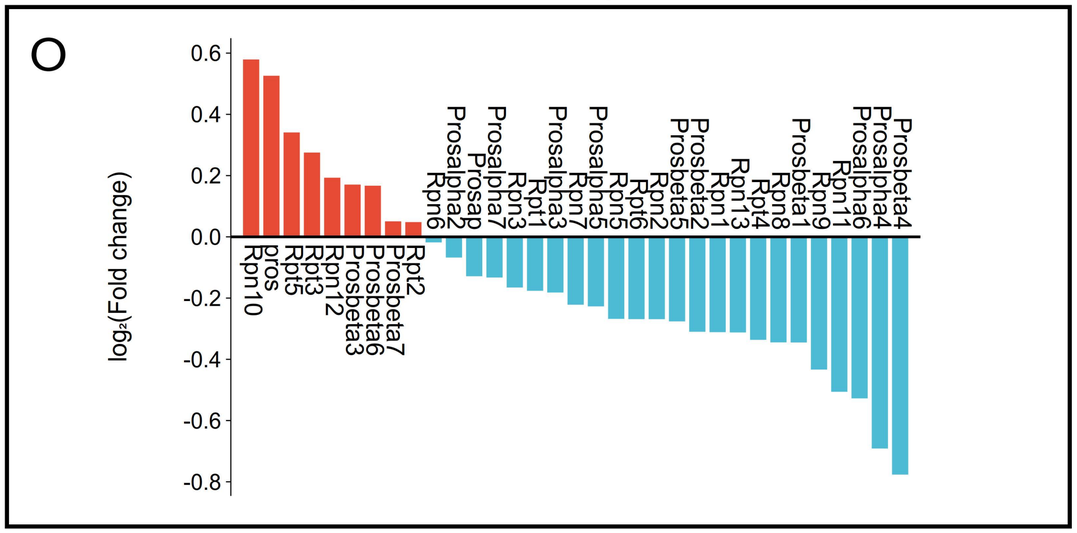

RNA and protein expression of per

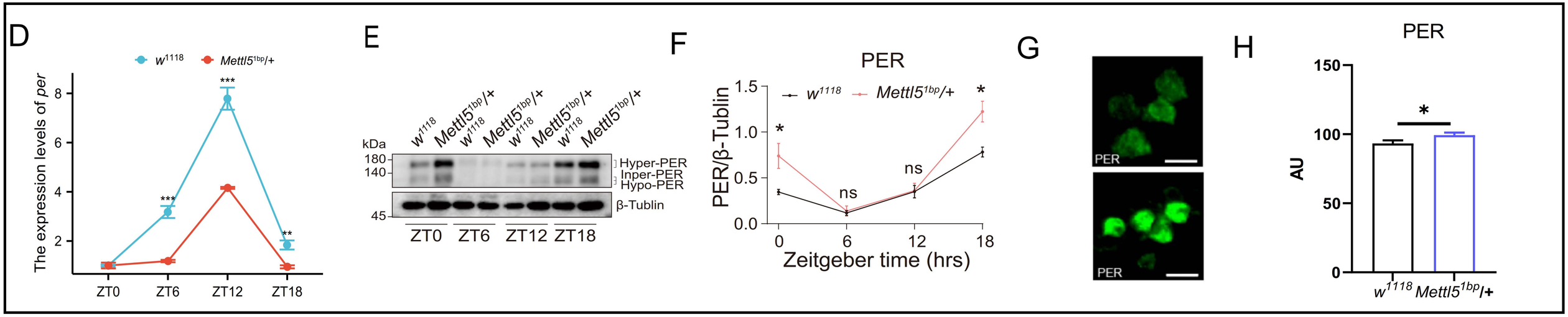

Genetic interactions

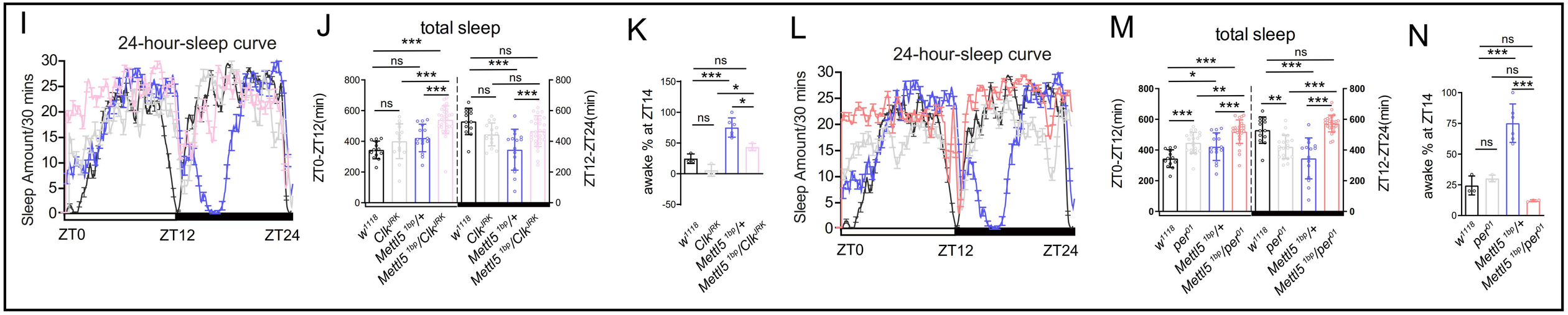

Figure5

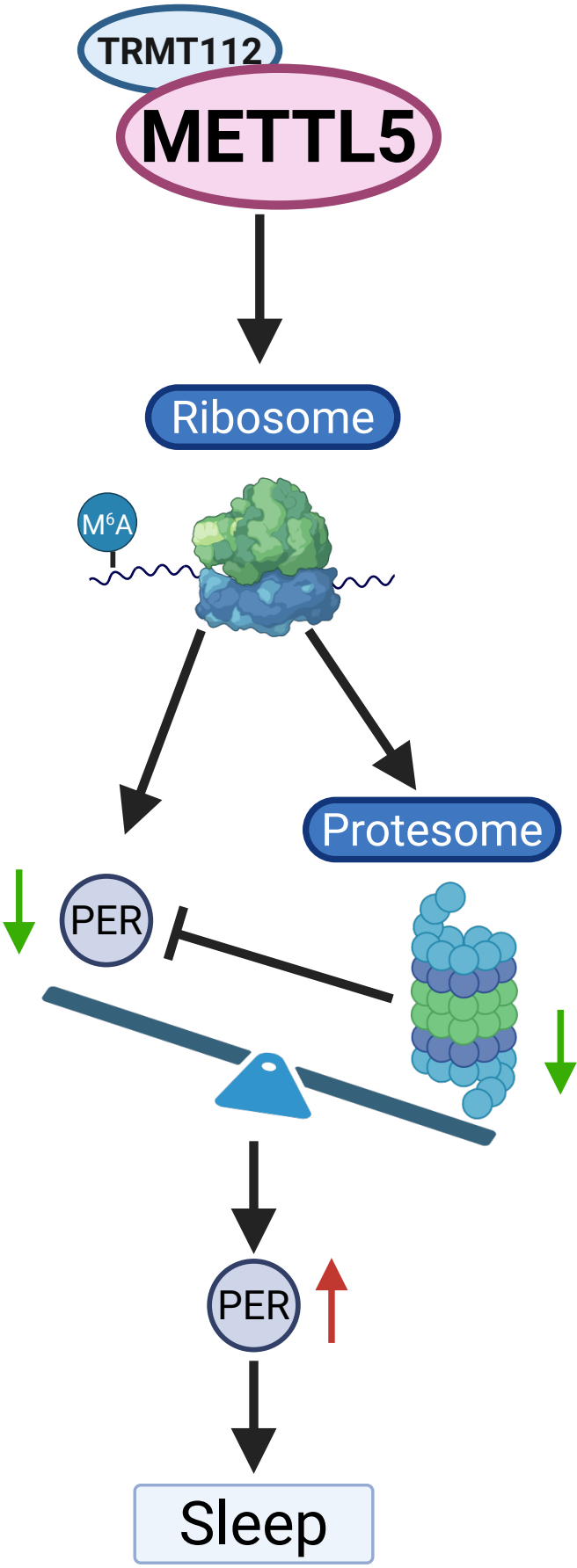

Figure 6

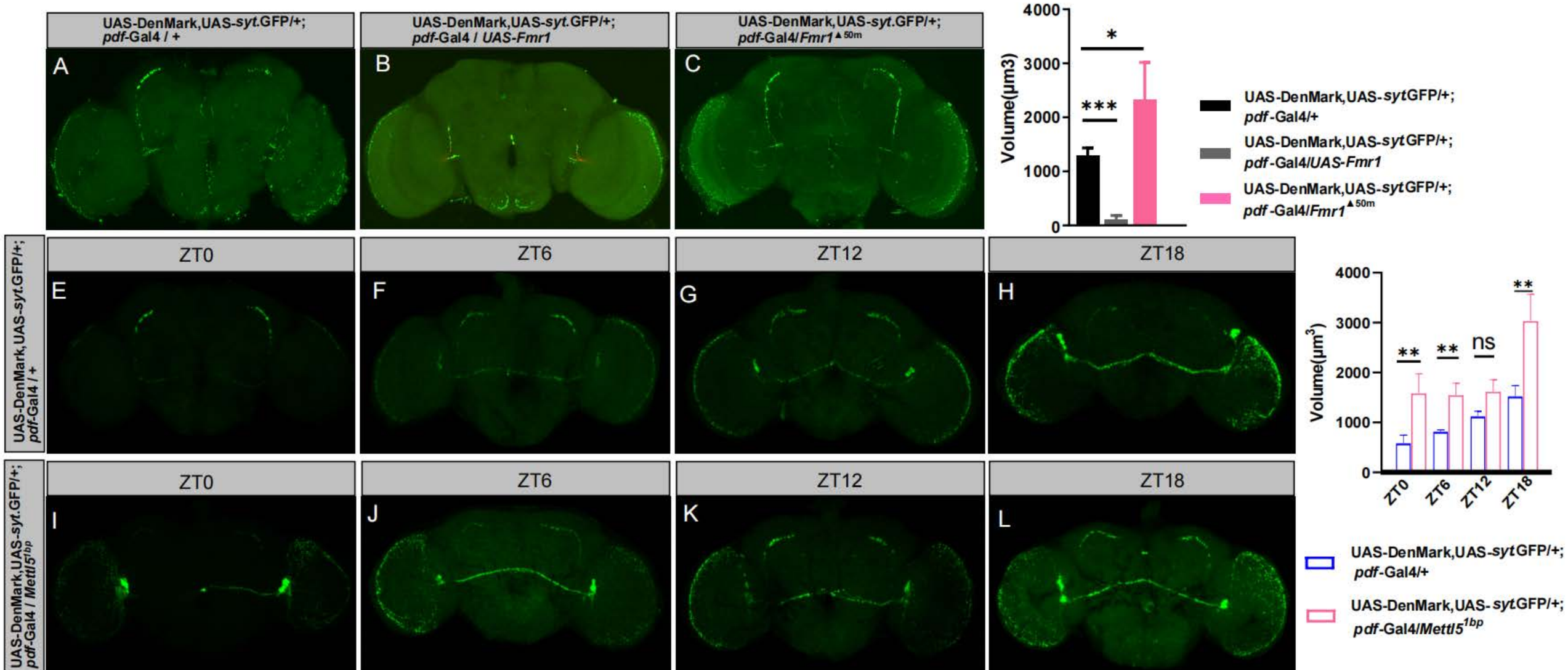
UAS-DenMark,UAS-syt.GFP/+; pdf-Gal4 / +
UAS-DenMark,UAS-syt.GFP/+; pdf-Gal4 / UAS-Fmr1
UAS-DenMark,UAS-syt.GFP/+; pdf-Gal4/Fmr1▲50m
A
B
C
Volume(µm3)
4000
3000
2000
1000
0
*
***
UAS-DenMark,UAS-sytGFP/+; pdf-Gal4/+
UAS-DenMark,UAS-sytGFP/+; pdf-Gal4/UAS-Fmr1
UAS-DenMark,UAS-sytGFP/+; pdf-Gal4/Fmr1▲50m
UAS-DenMark,UAS-syt.GFP/+; pdf-Gal4 / +
ZT0
ZT6
ZT12
ZT18
E
F
G
H
Volume(µm3)
**
**
ns
**
ZT0
ZT6
ZT12
ZT18
UAS-DenMark,UAS-syt.GFP/+; pdf-Gal4 / Mettl5^1bp
I
J
K
L
UAS-DenMark,UAS-sytGFP/+; pdf-Gal4/+
UAS-DenMark,UAS-sytGFP/+; pdf-Gal4/Mettl5^1bp

Genotype	NumTotal	%Rhythmic	Period	Power
w^{1118}	32	92.6	23.9± 0.05	127.9± 7.62
Mettl5 ^{1bp}/+	32	92.3	28.3± 0.4 ***	114.3± 6.76 ns
Mettl5 ^{1bp}/+ ; UAS-*Mettl5/Mettl5*Gal4	32	96.9	24± 0.02 ns	127.1± 5.42 ns
Mettl5 ^{1bp}/Clk^{JRK}	44	29.5	24± 0.04 ns	68.5± 8.85 ***
Mettl5 ^{1bp}/Per^{01}	54	9.3	24.2± 0.2 ns	43.8± 13.41 ***

Figure S1

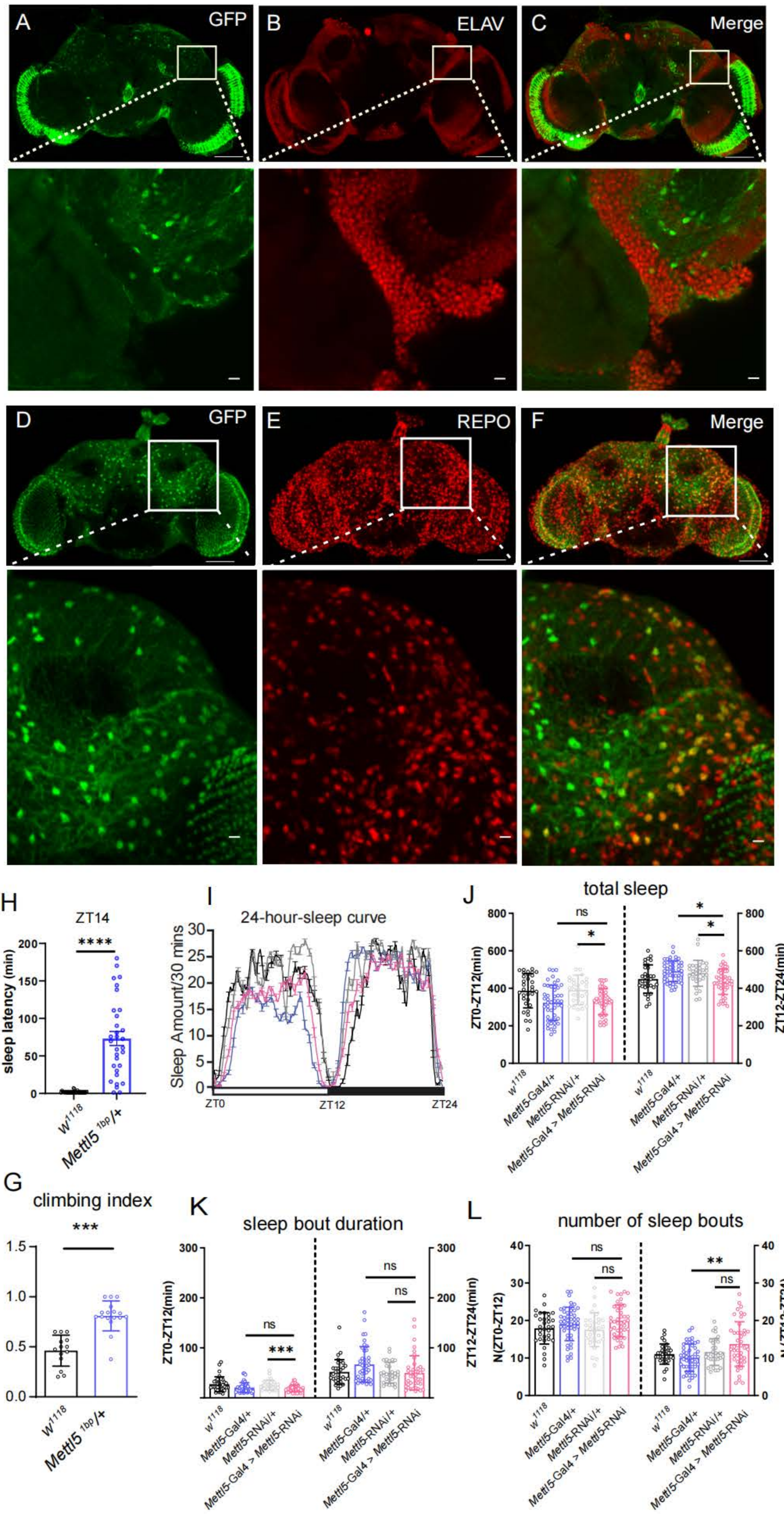
A
GFP
B
ELAV
C
Merge
D
GFP
E
REPO
F
Merge
H
ZT14
****
sleep latency (min)
200
150
100
50
0
w1118
Mettl5 1bp/+
I
24-hour-sleep curve
Sleep Amount/30 mins
30
25
20
15
10
5
0
ZT0
ZT12
ZT24
J
total sleep
ns
*
*
*
ZT0-ZT12(min)
ZT12-ZT24(min)
800
600
400
200
0
w1118
Mettl5-Gal4/+
Mettl5-RNAi/+
Mettl5-Gal4 > Mettl5-RNAi
G
climbing index
***
1.5
1.0
0.5
0.0
w1118
Mettl5 1bp/+
K
sleep bout duration
ZT0-ZT12(min)
ZT12-ZT24(min)
300
200
100
ns
***
ns
ns
w1118
Mettl5-Gal4/+
Mettl5-RNAi/+
Mettl5-Gal4 > Mettl5-RNAi
L
number of sleep bouts
N(ZT0-ZT12)
N (ZT12-ZT24)
40
30
20
10
0
ns
ns
**
ns
w1118
Mettl5-Gal4/+
Mettl5-RNAi/+
Mettl5-Gal4 > Mettl5-RNAi

Figure S2

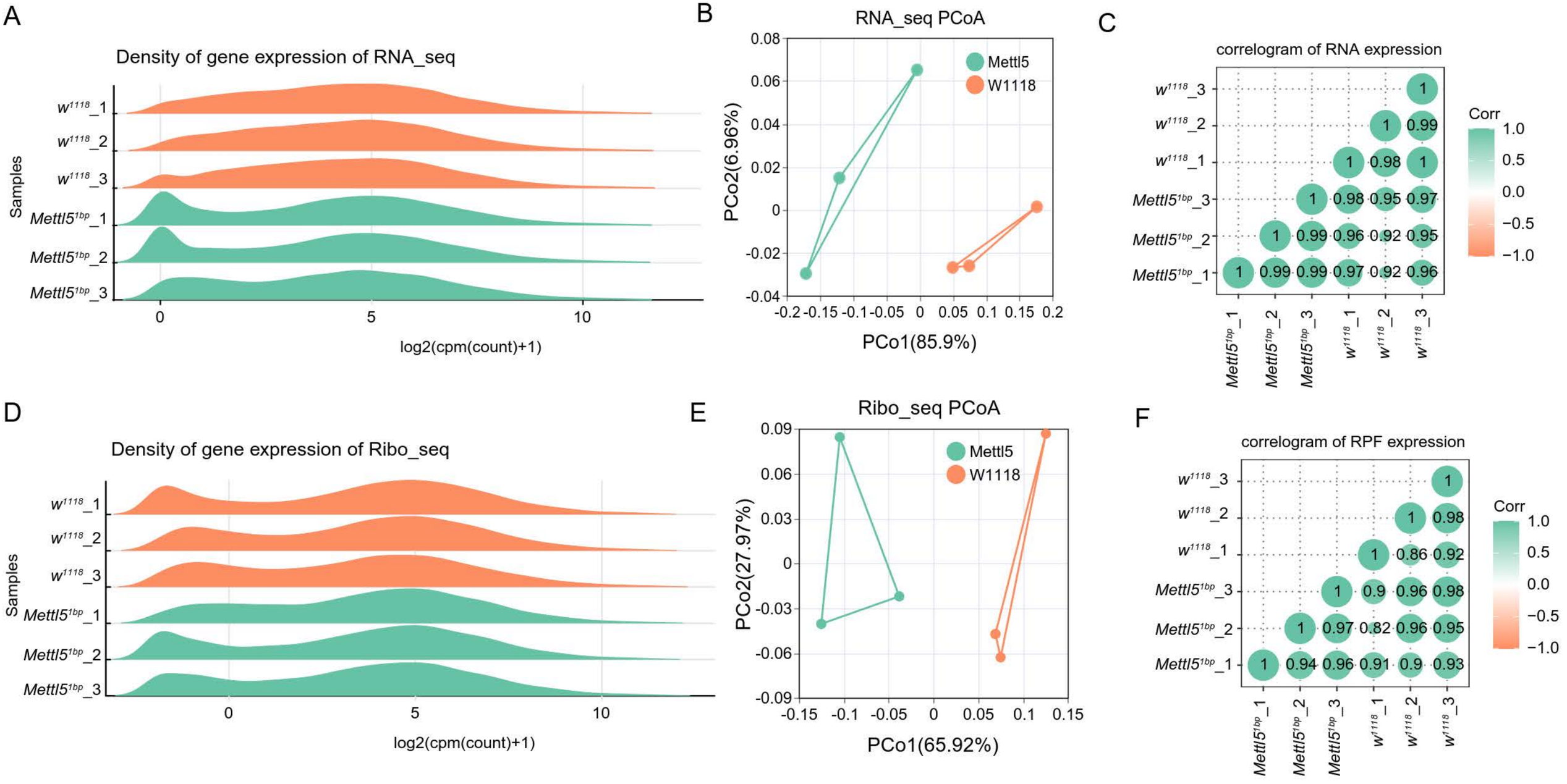
A
Density of gene expression of RNA_seq
Samples
w1118_1
w1118_2
w1118_3
Mettl5 1bp_1
Mettl5 1bp_2
Mettl5 1bp_3
0
5
10
log2(cpm(count)+1)
B
RNA_seq PCoA
Mettl5
W1118
PCo2(6.96%)
PCo1(85.9%)
C
correlogram of RNA expression
Corr
1.0
0.5
0.0
−0.5
−1.0
D
Density of gene expression of Ribo_seq
log2(cpm(count)+1)
E
Ribo_seq PCoA
PCo2(27.97%)
PCo1(65.92%)
F
correlogram of RPF expression

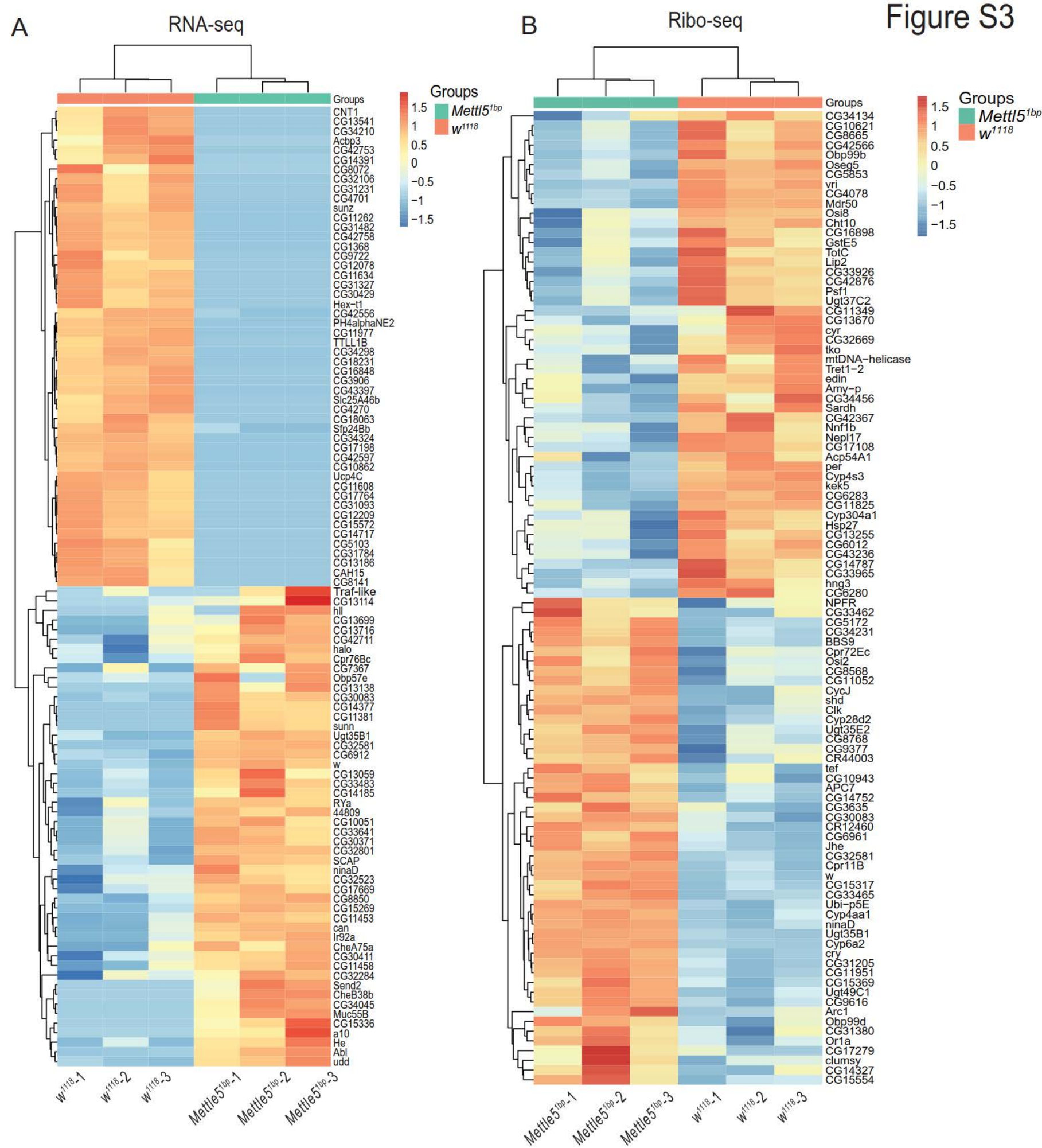
Figure S3
A
RNA-seq
Groups
Mettl5 1bp
w 1118
1.5
1
0.5
0
−0.5
−1
−1.5
Groups
CNT1
CG13541
CG34210
Acbp3
CG42753
CG14391
CG8072
CG32106
CG31231
CG4701
sunz
CG11262
CG31482
CG42758
CG1368
CG9722
CG12078
CG11634
CG31327
CG30429
Hex−t1
CG42556
PH4alphaNE2
CG11977
TTLL1B
CG34298
CG18231
CG16848
CG3906
CG43397
Slc25A46b
CG4270
CG18063
Sfp24Bb
CG34324
CG17198
CG42597
CG10862
Ucp4C
CG11608
CG17764
CG31093
CG12209
CG15572
CG14717
CG5103
CG31784
CG13186
CAH15
CG8141
Traf-like
CG13114
hll
CG13699
CG13716
CG42711
halo
Cpr76Bc
CG7367
Obp57e
CG13138
CG30083
CG14377
CG11381
sunn
Ugt35B1
CG32581
CG6912
w
CG13059
CG33483
CG14185
RYa
44809
CG10051
CG33641
CG30371
CG32801
SCAP
ninaD
CG32523
CG17669
CG8850
CG15269
CG11453
can
Ir92a
CheA75a
CG30411
CG11458
CG32284
Send2
CheB38b
CG34045
Muc55B
CG15336
a10
He
Abl
udd
w 1118 -1
w 1118 -2
w 1118 -3
Mettle5 1bp -1
Mettle5 1bp -2
Mettle5 1bp -3
B
Ribo-seq
Groups
Mettl5 1bp
w 1118
1.5
1
0.5
0
−0.5
−1
−1.5
Groups
CG34134
CG10621
CG8665
CG42566
Obp99b
Oseq5
CG5853
vri
CG4078
Mdr50
Osi8
Cht10
CG16898
GstE5
TotC
Lip2
CG33926
CG42876
Psf1
Ugt37C2
CG11349
CG13670
cyr
CG32669
tko
mtDNA−helicase
Tret1−2
edin
Amy−p
CG34456
Sardh
CG42367
Nnf1b
Nepl17
CG17108
Acp54A1
per
Cyp4s3
kek5
CG6283
CG11825
Cyp304a1
Hsp27
CG13255
CG6012
CG43236
CG14787
CG33965
hng3
CG6280
NPFR
CG33462
CG5172
CG34231
BBS9
Cpr72Ec
Osi2
CG8568
CG11052
CycJ
shd
Clk
Cyp28d2
Ugt35E2
CG8768
CG9377
CR44003
tef
CG10943
APC7
CG14752
CG3635
CG30083
CR12460
CG6961
Jhe
CG32581
Cpr11B
w
CG15317
CG33465
Ubi−p5E
Cyp4aa1
ninaD
Ugt35B1
Cyp6a2
cry
CG31205
CG11951
CG15369
Ugt49C1
CG9616
Arc1
Obp99d
CG31380
Or1a
CG17279
clumsy
CG14327
CG15554
Mettle5 1bp -1
Mettle5 1bp -2
Mettle5 1bp -3
w 1118 -1
w 1118 -2
w 1118 -3

Figure S4

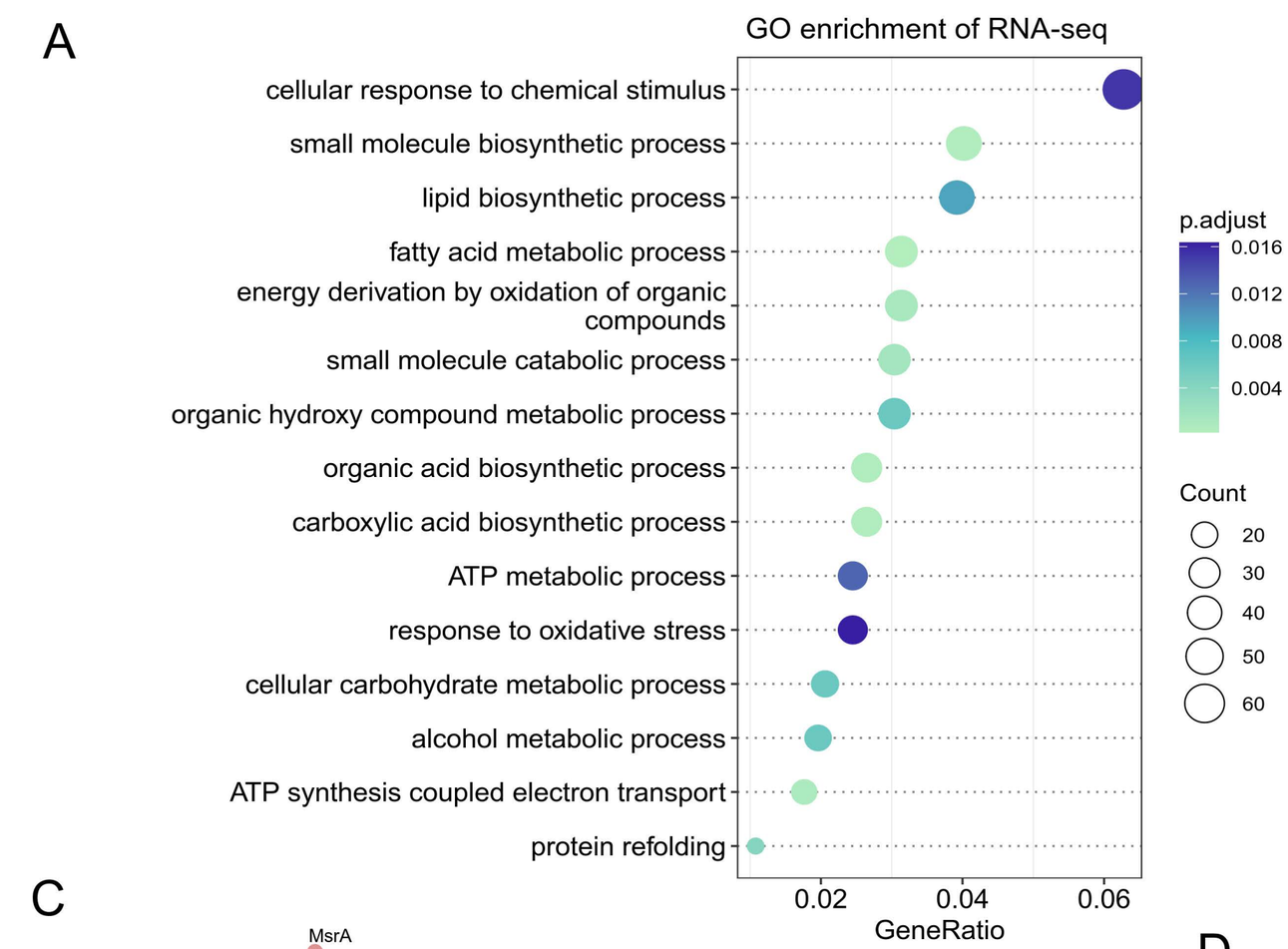
A
GO enrichment of RNA-seq
cellular response to chemical stimulus
small molecule biosynthetic process
lipid biosynthetic process
fatty acid metabolic process
energy derivation by oxidation of organic compounds
small molecule catabolic process
organic hydroxy compound metabolic process
organic acid biosynthetic process
carboxylic acid biosynthetic process
ATP metabolic process
response to oxidative stress
cellular carbohydrate metabolic process
alcohol metabolic process
ATP synthesis coupled electron transport
protein refolding
0.02
0.04
0.06
GeneRatio
p.adjust
0.016
0.012
0.008
0.004
Count
20
30
40
50
60

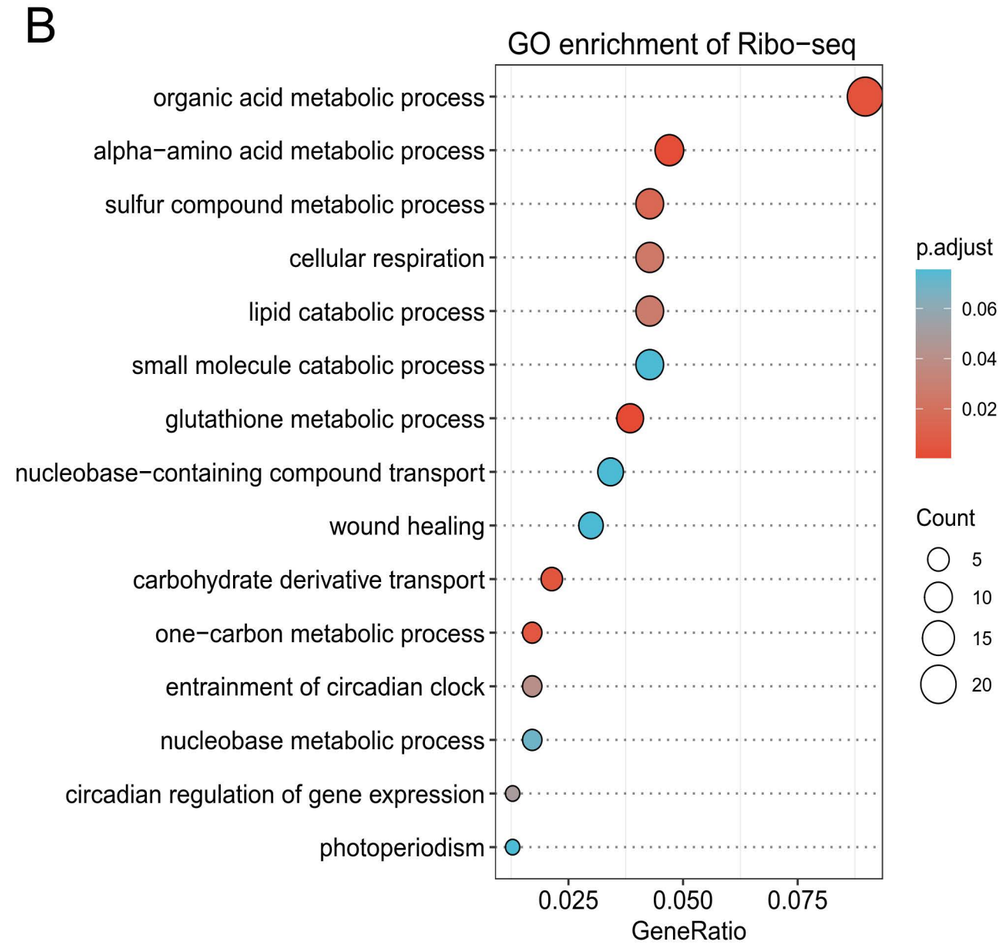
B
GO enrichment of Ribo−seq
organic acid metabolic process
alpha−amino acid metabolic process
sulfur compound metabolic process
cellular respiration
lipid catabolic process
small molecule catabolic process
glutathione metabolic process
nucleobase−containing compound transport
wound healing
carbohydrate derivative transport
one−carbon metabolic process
entrainment of circadian clock
nucleobase metabolic process
circadian regulation of gene expression
photoperiodism
0.025
0.050
0.075
GeneRatio
p.adjust
0.06
0.04
0.02
Count
5
10
15
20

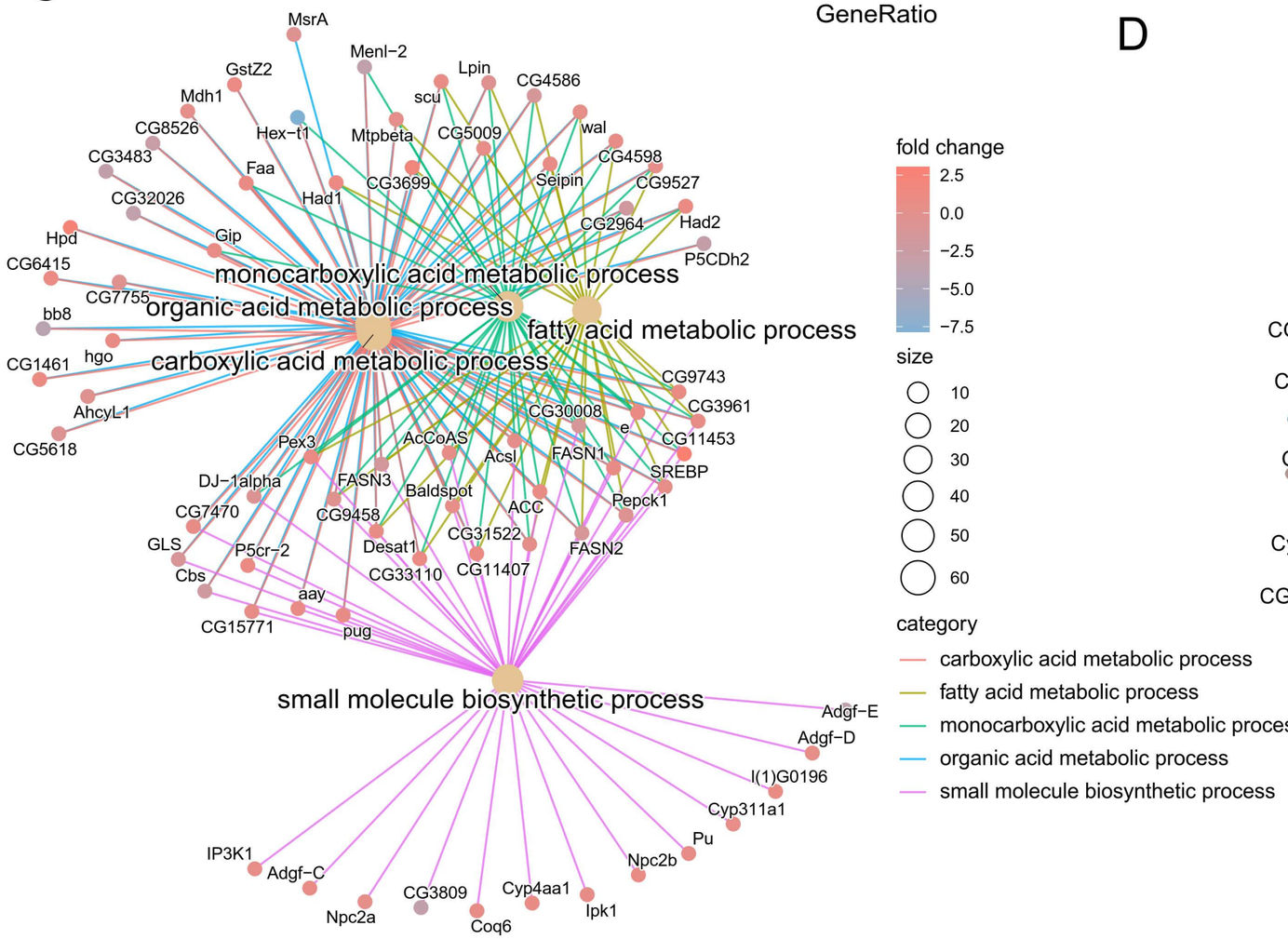
C
MsrA
Menl−2
GstZ2
Lpin
CG4586
Mdh1
scu
CG8526
Hex−t1
Mtpbeta
CG5009
wal
CG3483
CG4598
Faa
CG3699
Seipin
CG9527
CG32026
Had1
CG2964
Had2
Hpd
Gip
P5CDh2
CG6415
monocarboxylic acid metabolic process
CG7755
organic acid metabolic process
fatty acid metabolic process
bb8
CG1461
hgo
carboxylic acid metabolic process
CG9743
CG3961
AhcyL1
CG30008
e
CG11453
CG5618
Pex3
AcCoAS
Acsl
FASN1
SREBP
DJ−1alpha
FASN3
Baldspot
ACC
Pepck1
CG7470
CG9458
CG31522
GLS
P5cr−2
Desat1
FASN2
Cbs
CG33110
CG11407
aay
CG15771
pug
small molecule biosynthetic process
Adgf−E
Adgf−D
l(1)G0196
Cyp311a1
Pu
IP3K1
Adgf−C
Npc2b
CG3809
Cyp4aa1
Npc2a
Ipk1
Coq6
fold change
2.5
0.0
−2.5
−5.0
−7.5
size
10
20
30
40
50
60
category
carboxylic acid metabolic process
fatty acid metabolic process
monocarboxylic acid metabolic process
organic acid metabolic process
small molecule biosynthetic process

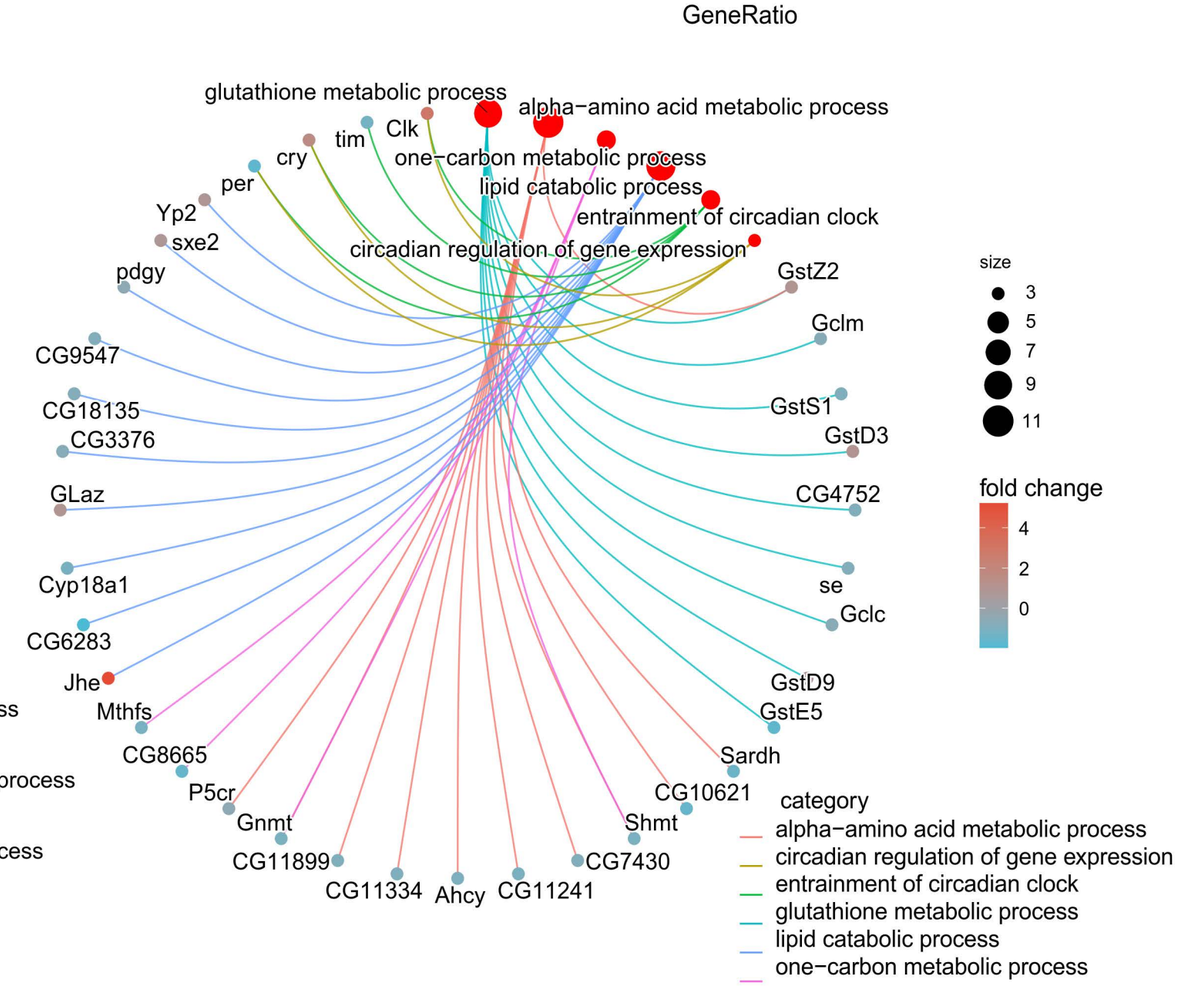
D
glutathione metabolic process
alpha−amino acid metabolic process
Clk
tim
cry
one−carbon metabolic process
per
lipid catabolic process
Yp2
entrainment of circadian clock
sxe2
circadian regulation of gene expression
pdgy
GstZ2
Gclm
CG9547
CG18135
GstS1
CG3376
GstD3
GLaz
CG4752
Cyp18a1
se
Gclc
CG6283
Jhe
GstD9
Mthfs
GstE5
CG8665
Sardh
P5cr
CG10621
Gnmt
Shmt
CG11899
CG7430
CG11334
Ahcy
CG11241
size
3
5
7
9
11
fold change
4
2
0
category
alpha−amino acid metabolic process
circadian regulation of gene expression
entrainment of circadian clock
glutathione metabolic process
lipid catabolic process
one−carbon metabolic process

Figure S5

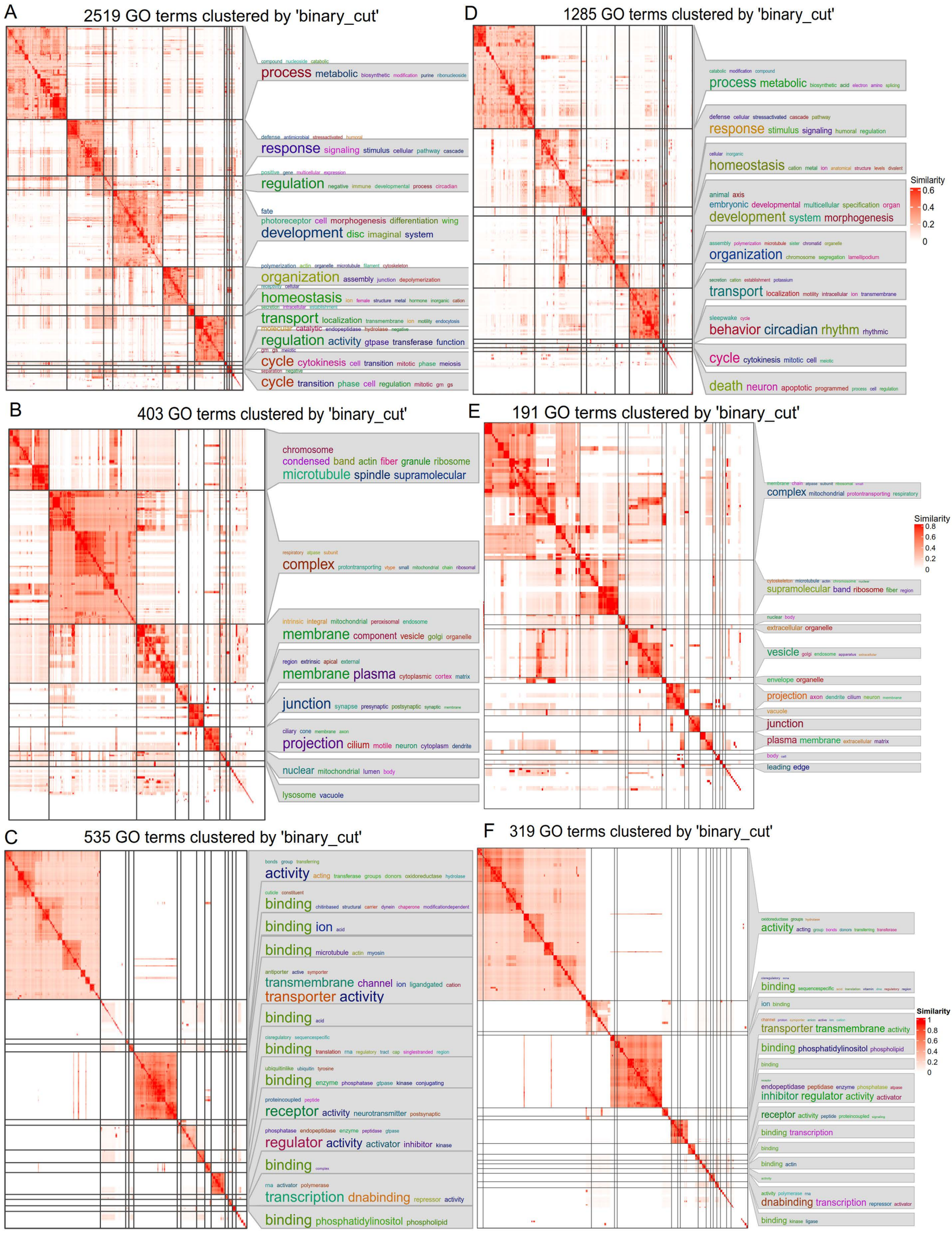
A
2519 GO terms clustered by 'binary_cut'
process metabolic
response signaling stimulus cellular pathway cascade
regulation
development disc imaginal system
organization assembly
homeostasis
transport localization
regulation activity gtpase transferase function
cycle cytokinesis cell transition mitotic phase meiosis
cycle transition phase cell regulation mitotic gm gs
D
1285 GO terms clustered by 'binary_cut'
process metabolic
response stimulus signaling humoral regulation
homeostasis
development system morphogenesis
organization
transport localization
behavior circadian rhythm
cycle cytokinesis mitotic cell
death neuron apoptotic programmed
Similarity
0.6
0.4
0.2
0
B
403 GO terms clustered by 'binary_cut'
chromosome
condensed band actin fiber granule ribosome
microtubule spindle supramolecular
complex
membrane component vesicle golgi organelle
membrane plasma cytoplasmic cortex matrix
junction synapse presynaptic postsynaptic
projection cilium motile neuron cytoplasm dendrite
nuclear mitochondrial lumen body
lysosome vacuole
E
191 GO terms clustered by 'binary_cut'
complex mitochondrial protontransporting respiratory
supramolecular band ribosome fiber region
extracellular organelle
vesicle
envelope organelle
projection axon dendrite cilium neuron
junction
plasma membrane extracellular matrix
leading edge
Similarity
0.8
0.6
0.4
0.2
0
C
535 GO terms clustered by 'binary_cut'
activity acting transferase groups donors oxidoreductase hydrolase
binding
binding ion
binding microtubule
transmembrane channel ion ligandgated
transporter activity
binding
binding
binding enzyme phosphatase gtpase kinase conjugating
receptor activity neurotransmitter postsynaptic
regulator activity activator inhibitor kinase
binding
transcription dnabinding repressor activity
binding phosphatidylinositol phospholipid
F
319 GO terms clustered by 'binary_cut'
activity
binding
ion binding
transporter transmembrane activity
binding phosphatidylinositol phospholipid
inhibitor regulator activity activator
receptor activity
binding transcription
binding actin
dnabinding transcription repressor activator
binding kinase ligase
Similarity
1
0.8
0.6
0.4
0.2
0

Figure S6

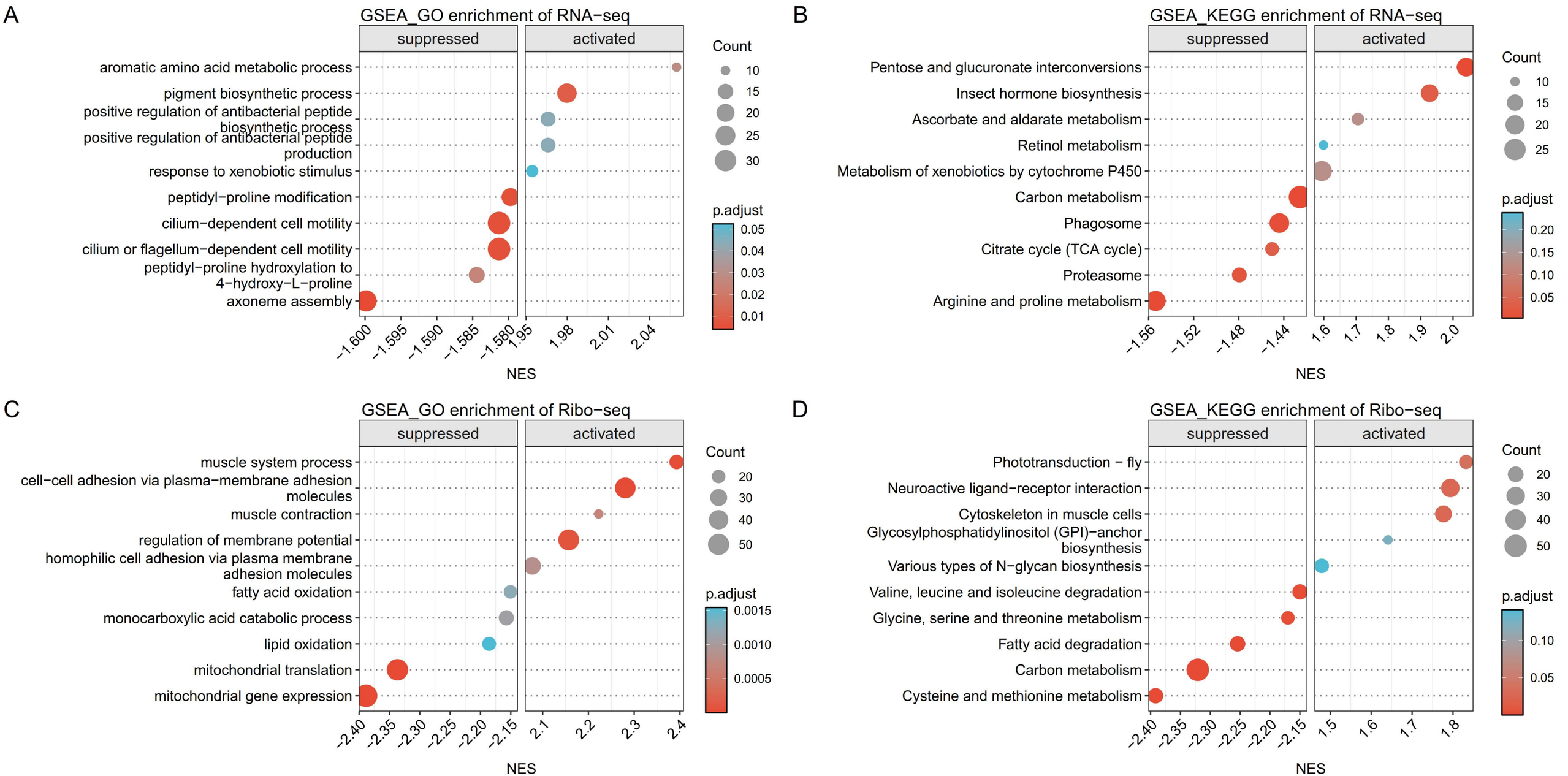
A
GSEA_GO enrichment of RNA−seq
suppressed
activated
aromatic amino acid metabolic process
pigment biosynthetic process
positive regulation of antibacterial peptide biosynthetic process
positive regulation of antibacterial peptide production
response to xenobiotic stimulus
peptidyl−proline modification
cilium−dependent cell motility
cilium or flagellum−dependent cell motility
peptidyl−proline hydroxylation to 4−hydroxy−L−proline
axoneme assembly
−1.600
−1.595
−1.590
−1.585
−1.580
1.95
1.98
2.01
2.04
NES
Count
10
15
20
25
30
p.adjust
0.05
0.04
0.03
0.02
0.01
B
GSEA_KEGG enrichment of RNA−seq
suppressed
activated
Pentose and glucuronate interconversions
Insect hormone biosynthesis
Ascorbate and aldarate metabolism
Retinol metabolism
Metabolism of xenobiotics by cytochrome P450
Carbon metabolism
Phagosome
Citrate cycle (TCA cycle)
Proteasome
Arginine and proline metabolism
−1.56
−1.52
−1.48
−1.44
1.6
1.7
1.8
1.9
2.0
NES
Count
10
15
20
25
p.adjust
0.20
0.15
0.10
0.05
C
GSEA_GO enrichment of Ribo−seq
suppressed
activated
muscle system process
cell−cell adhesion via plasma−membrane adhesion molecules
muscle contraction
regulation of membrane potential
homophilic cell adhesion via plasma membrane adhesion molecules
fatty acid oxidation
monocarboxylic acid catabolic process
lipid oxidation
mitochondrial translation
mitochondrial gene expression
−2.40
−2.35
−2.30
−2.25
−2.20
−2.15
2.1
2.2
2.3
2.4
NES
Count
20
30
40
50
p.adjust
0.0015
0.0010
0.0005
D
GSEA_KEGG enrichment of Ribo−seq
suppressed
activated
Phototransduction − fly
Neuroactive ligand−receptor interaction
Cytoskeleton in muscle cells
Glycosylphosphatidylinositol (GPI)−anchor biosynthesis
Various types of N−glycan biosynthesis
Valine, leucine and isoleucine degradation
Glycine, serine and threonine metabolism
Fatty acid degradation
Carbon metabolism
Cysteine and methionine metabolism
−2.40
−2.35
−2.30
−2.25
−2.20
−2.15
1.5
1.6
1.7
1.8
NES
Count
20
30
40
50
p.adjust
0.10
0.05

Figure S7

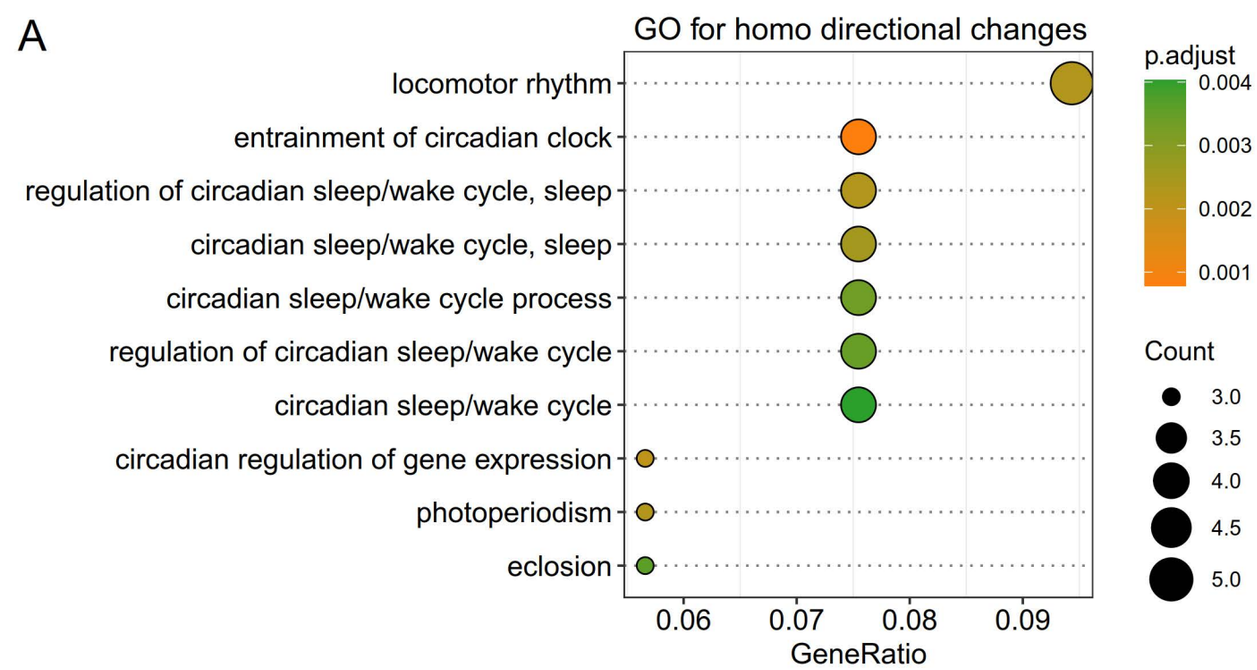
A
GO for homo directional changes
locomotor rhythm
entrainment of circadian clock
regulation of circadian sleep/wake cycle, sleep
circadian sleep/wake cycle, sleep
circadian sleep/wake cycle process
regulation of circadian sleep/wake cycle
circadian sleep/wake cycle
circadian regulation of gene expression
photoperiodism
eclosion
0.06 0.07 0.08 0.09
GeneRatio
p.adjust
0.004 0.003 0.002 0.001
Count
3.0 3.5 4.0 4.5 5.0

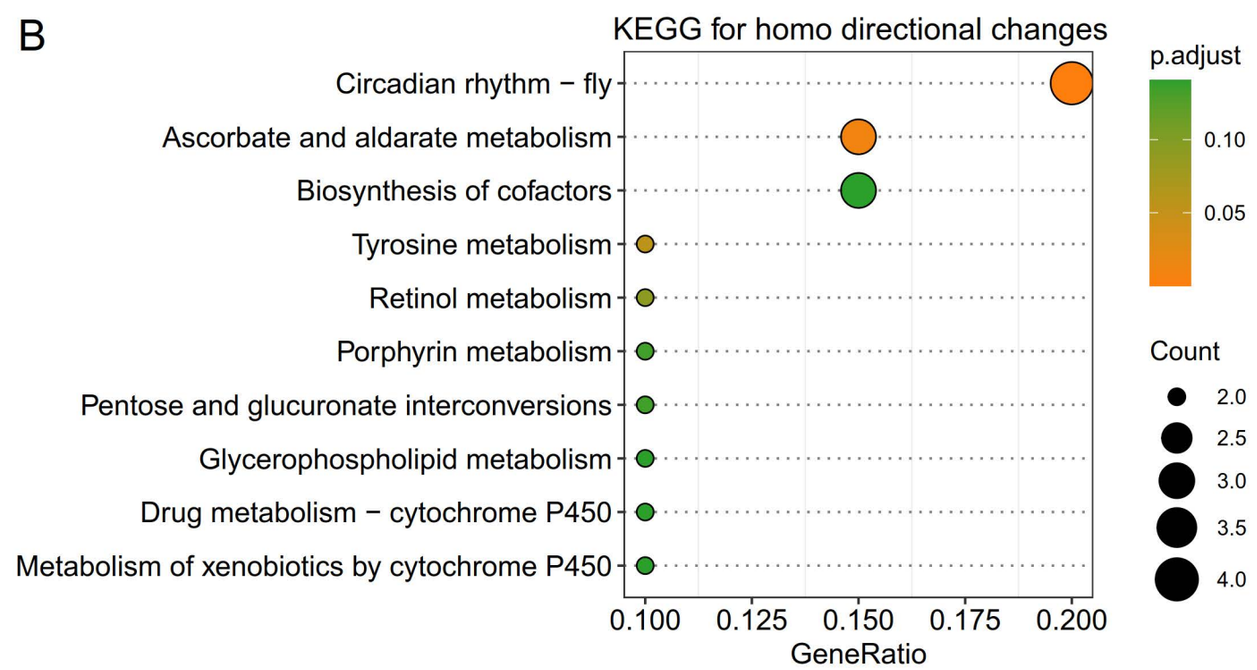
B
KEGG for homo directional changes
Circadian rhythm − fly
Ascorbate and aldarate metabolism
Biosynthesis of cofactors
Tyrosine metabolism
Retinol metabolism
Porphyrin metabolism
Pentose and glucuronate interconversions
Glycerophospholipid metabolism
Drug metabolism − cytochrome P450
Metabolism of xenobiotics by cytochrome P450
0.100 0.125 0.150 0.175 0.200
GeneRatio
p.adjust
0.10 0.05
Count
2.0 2.5 3.0 3.5 4.0

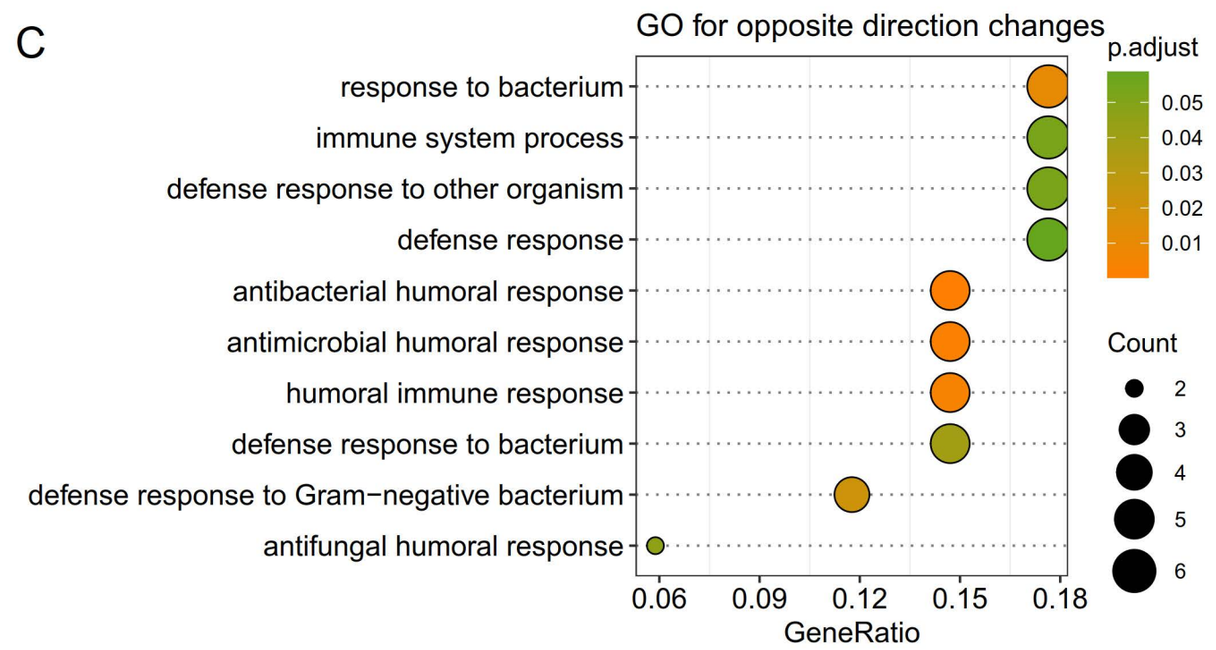
C
GO for opposite direction changes
response to bacterium
immune system process
defense response to other organism
defense response
antibacterial humoral response
antimicrobial humoral response
humoral immune response
defense response to bacterium
defense response to Gram−negative bacterium
antifungal humoral response
0.06 0.09 0.12 0.15 0.18
GeneRatio
p.adjust
0.05 0.04 0.03 0.02 0.01
Count
2 3 4 5 6

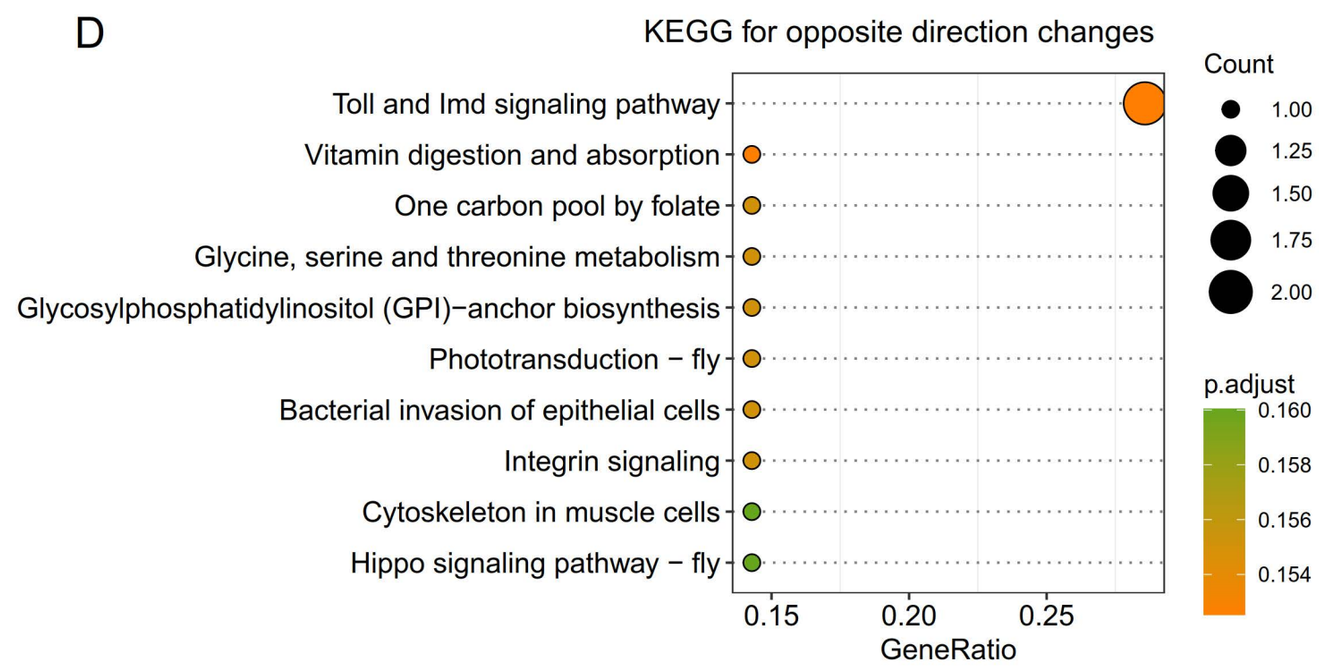
D
KEGG for opposite direction changes
Toll and Imd signaling pathway
Vitamin digestion and absorption
One carbon pool by folate
Glycine, serine and threonine metabolism
Glycosylphosphatidylinositol (GPI)−anchor biosynthesis
Phototransduction − fly
Bacterial invasion of epithelial cells
Integrin signaling
Cytoskeleton in muscle cells
Hippo signaling pathway − fly
0.15 0.20 0.25
GeneRatio
Count
1.00 1.25 1.50 1.75 2.00
p.adjust
0.160 0.158 0.156 0.154

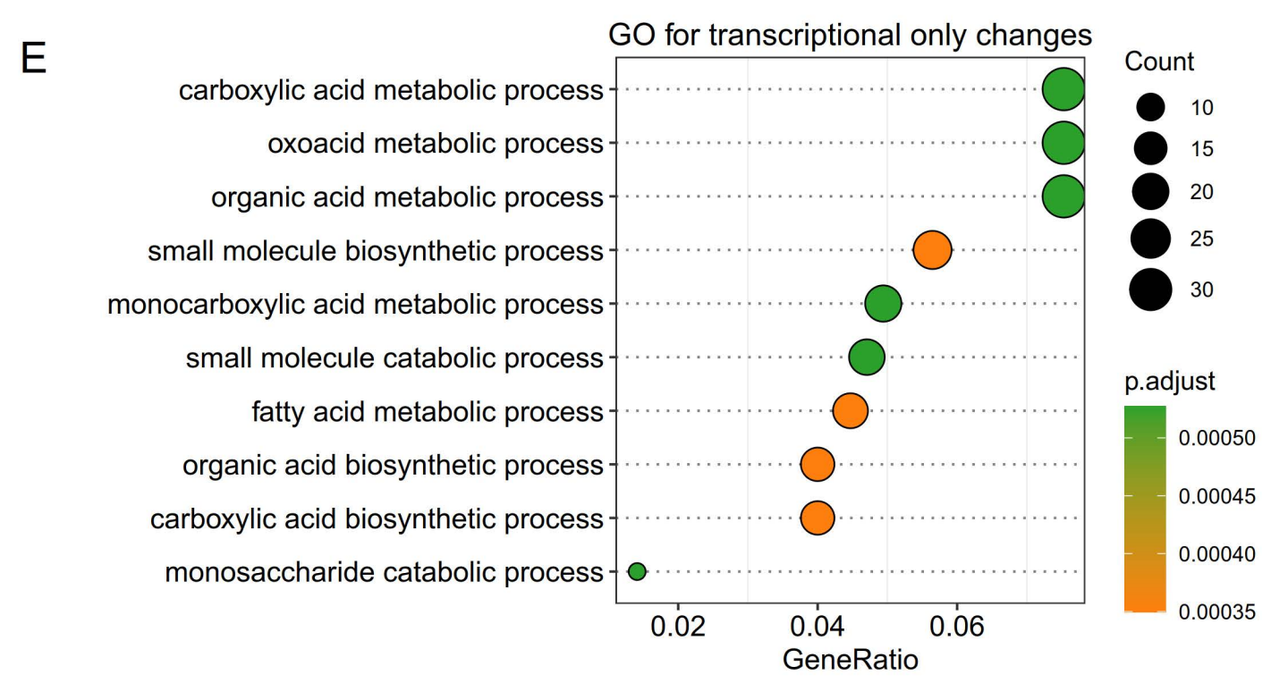
E
GO for transcriptional only changes
carboxylic acid metabolic process
oxoacid metabolic process
organic acid metabolic process
small molecule biosynthetic process
monocarboxylic acid metabolic process
small molecule catabolic process
fatty acid metabolic process
organic acid biosynthetic process
carboxylic acid biosynthetic process
monosaccharide catabolic process
0.02 0.04 0.06
GeneRatio
Count
10 15 20 25 30
p.adjust
0.00050 0.00045 0.00040 0.00035

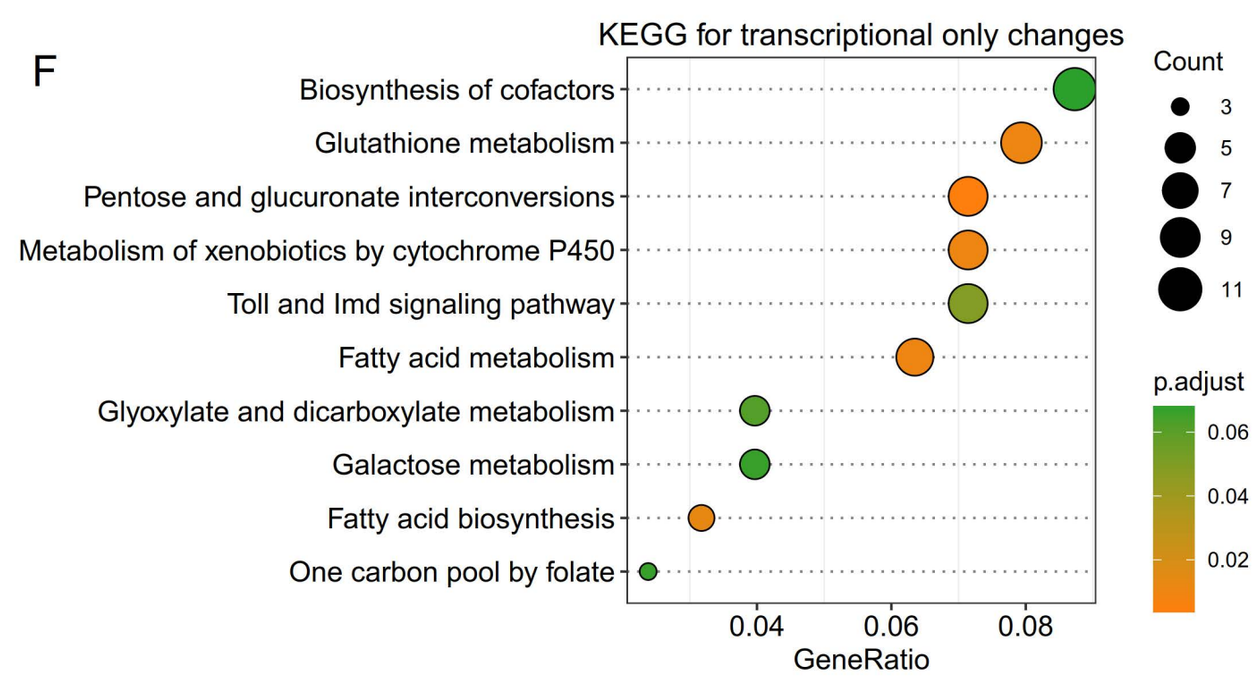
F
KEGG for transcriptional only changes
Biosynthesis of cofactors
Glutathione metabolism
Pentose and glucuronate interconversions
Metabolism of xenobiotics by cytochrome P450
Toll and Imd signaling pathway
Fatty acid metabolism
Glyoxylate and dicarboxylate metabolism
Galactose metabolism
Fatty acid biosynthesis
One carbon pool by folate
0.04 0.06 0.08
GeneRatio
Count
3 5 7 9 11
p.adjust
0.06 0.04 0.02

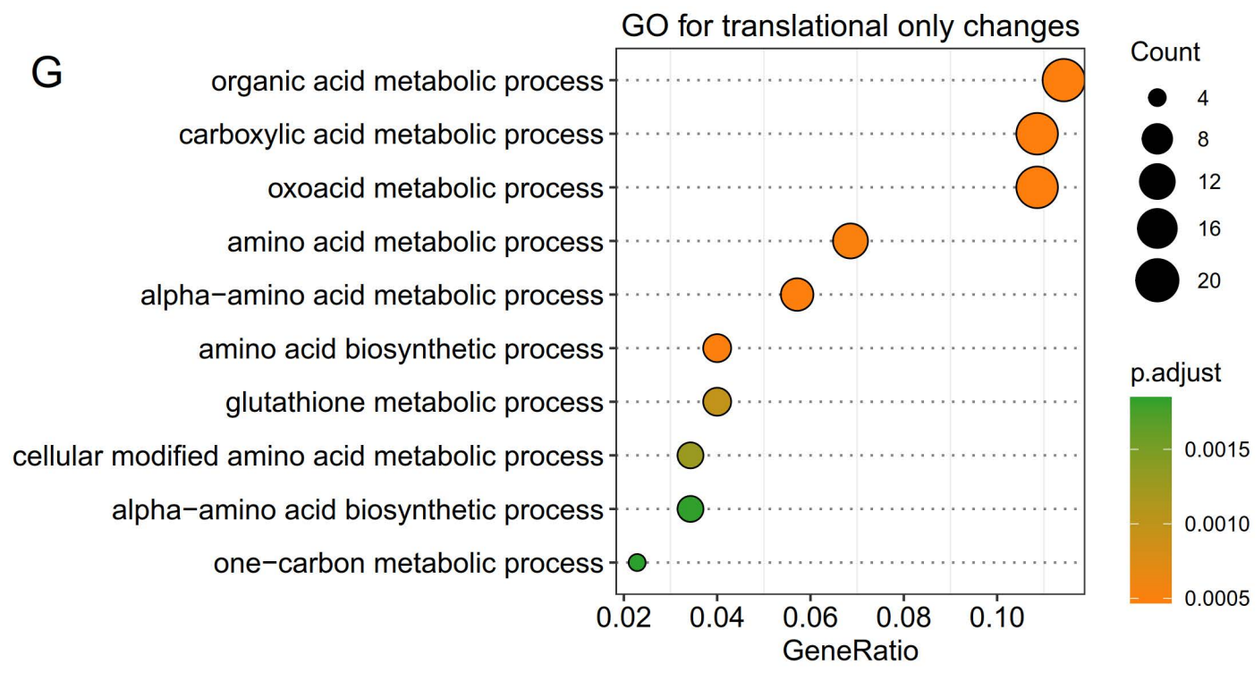
G
GO for translational only changes
organic acid metabolic process
carboxylic acid metabolic process
oxoacid metabolic process
amino acid metabolic process
alpha−amino acid metabolic process
amino acid biosynthetic process
glutathione metabolic process
cellular modified amino acid metabolic process
alpha−amino acid biosynthetic process
one−carbon metabolic process
0.02 0.04 0.06 0.08 0.10
GeneRatio
Count
4 8 12 16 20
p.adjust
0.0015 0.0010 0.0005

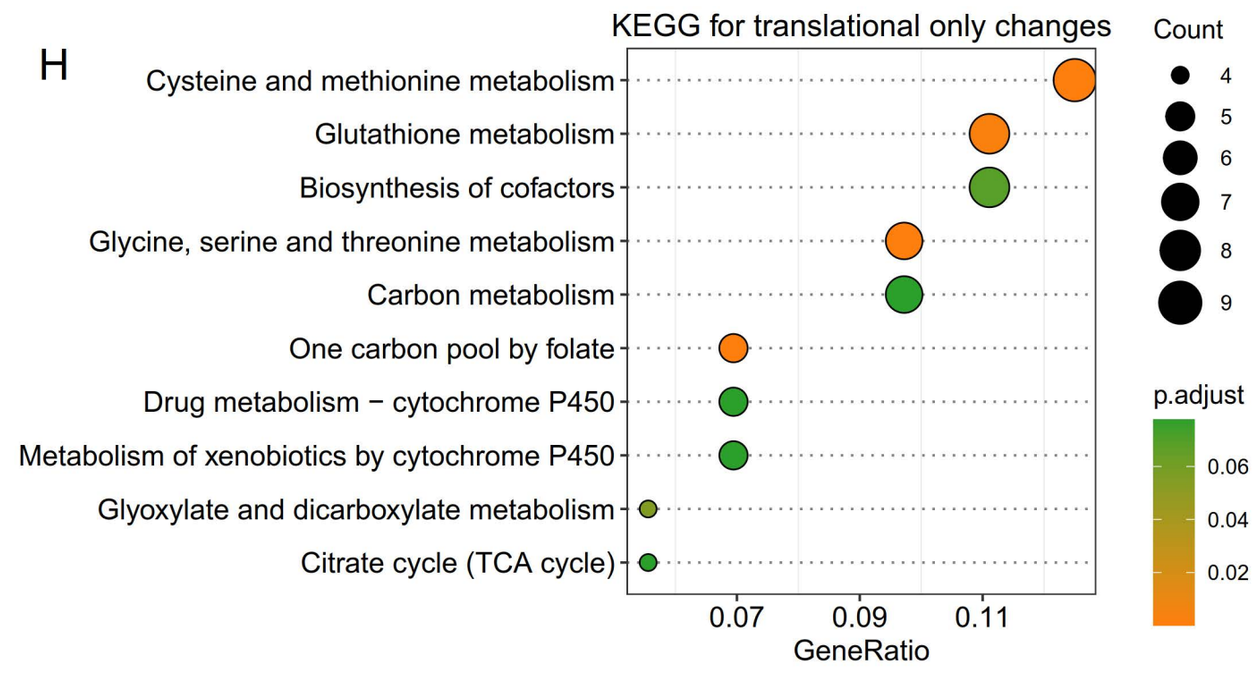
H
KEGG for translational only changes
Cysteine and methionine metabolism
Glutathione metabolism
Biosynthesis of cofactors
Glycine, serine and threonine metabolism
Carbon metabolism
One carbon pool by folate
Drug metabolism − cytochrome P450
Metabolism of xenobiotics by cytochrome P450
Glyoxylate and dicarboxylate metabolism
Citrate cycle (TCA cycle)
0.07 0.09 0.11
GeneRatio
Count
4 5 6 7 8 9
p.adjust
0.06 0.04 0.02

Figure S8

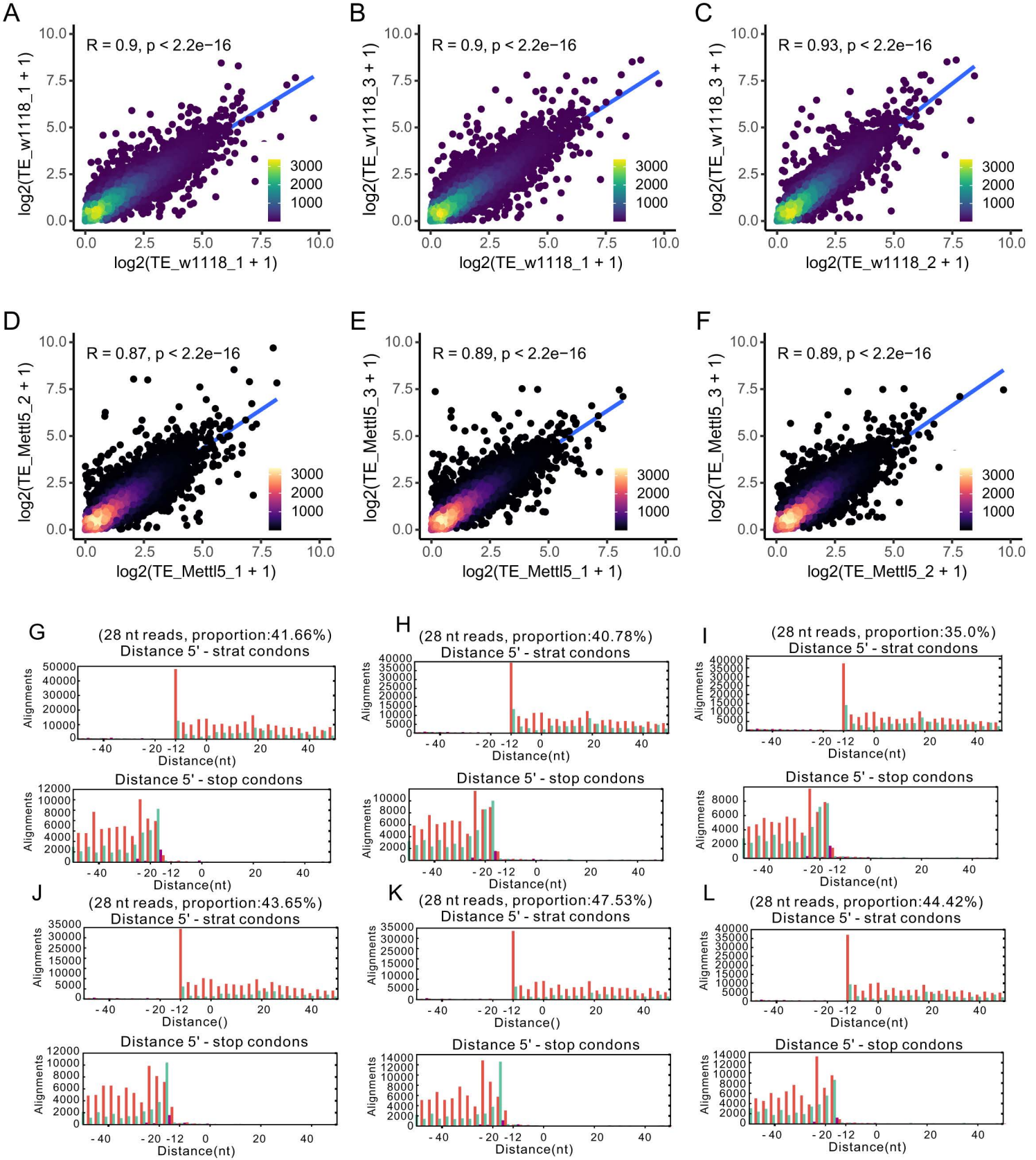
A
R = 0.9, p < 2.2e−16
log2(TE_w1118_1 + 1)
log2(TE_w1118_1 + 1)
B
R = 0.9, p < 2.2e−16
log2(TE_w1118_3 + 1)
log2(TE_w1118_1 + 1)
C
R = 0.93, p < 2.2e−16
log2(TE_w1118_3 + 1)
log2(TE_w1118_2 + 1)
D
R = 0.87, p < 2.2e−16
log2(TE_Mettl5_2 + 1)
log2(TE_Mettl5_1 + 1)
E
R = 0.89, p < 2.2e−16
log2(TE_Mettl5_3 + 1)
log2(TE_Mettl5_1 + 1)
F
R = 0.89, p < 2.2e−16
log2(TE_Mettl5_3 + 1)
log2(TE_Mettl5_2 + 1)
G
(28 nt reads, proportion:41.66%)
Distance 5' - strat condons
Distance 5' - stop condons
H
(28 nt reads, proportion:40.78%)
Distance 5' - strat condons
Distance 5' - stop condons
I
(28 nt reads, proportion:35.0%)
Distance 5' - strat condons
Distance 5' - stop condons
J
(28 nt reads, proportion:43.65%)
Distance 5' - strat condons
Distance 5' - stop condons
K
(28 nt reads, proportion:47.53%)
Distance 5' - strat condons
Distance 5' - stop condons
L
(28 nt reads, proportion:44.42%)
Distance 5' - strat condons
Distance 5' - stop condons
Alignments
Distance(nt)

Figure S9

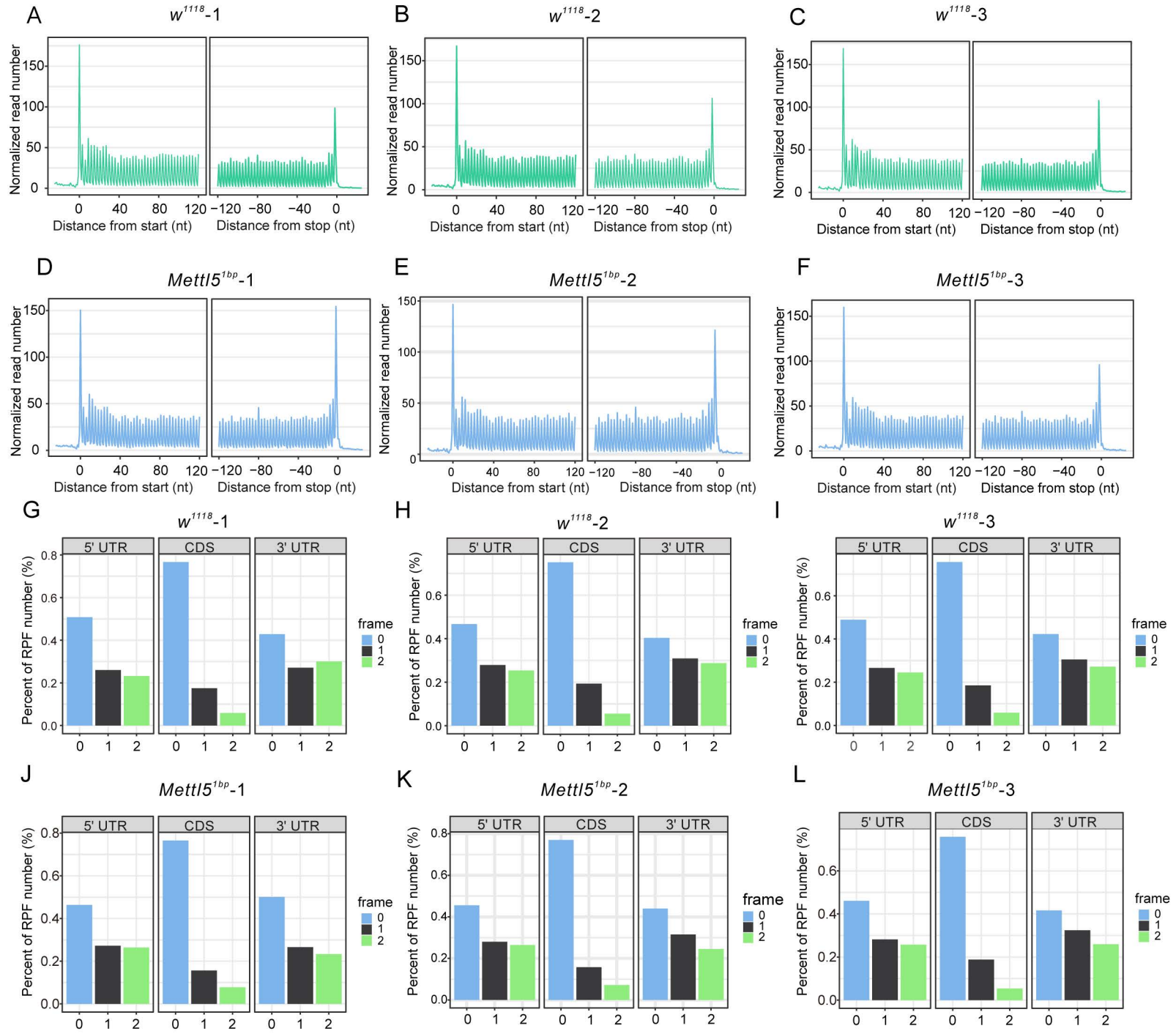
A
w1118-1
B
w1118-2
C
w1118-3
D
Mettl5 1bp-1
E
Mettl5 1bp-2
F
Mettl5 1bp-3
Normalized read number
Distance from start (nt)
Distance from stop (nt)
G
w1118-1
H
w1118-2
I
w1118-3
J
Mettl5 1bp-1
K
Mettl5 1bp-2
L
Mettl5 1bp-3
5' UTR
CDS
3' UTR
Percent of RPF number (%)
frame
0
1
2

Figure S10

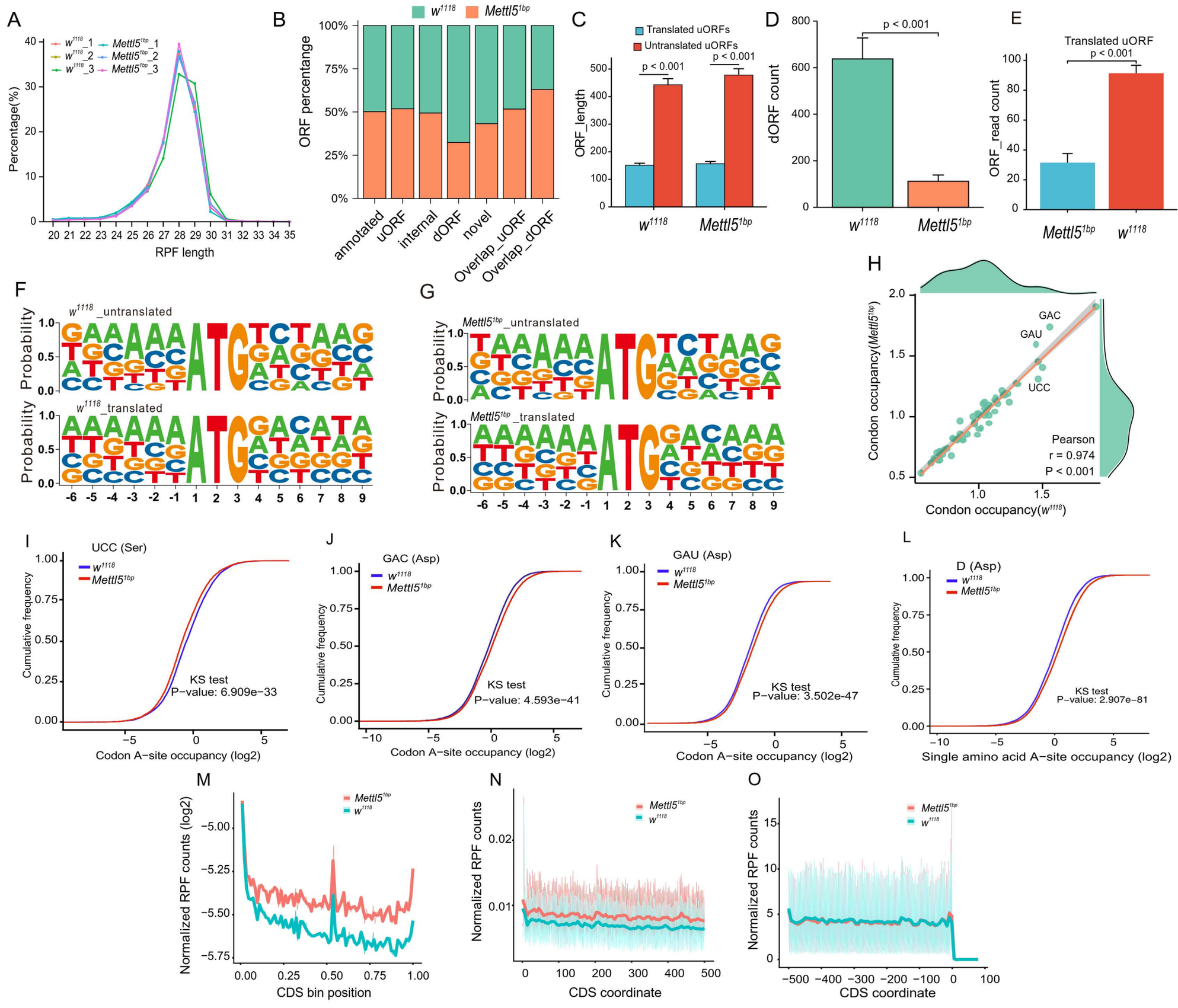
A
Percentage(%)
RPF length
B
ORF percentage
annotated
uORF
internal
dORF
novel
Overlap_uORF
Overlap_dORF
C
Translated uORFs
Untranslated uORFs
p < 0.001
ORF_length
D
dORF count
E
Translated uORF
ORF_read count
F
G
H
Condon occupancy(Mettl5 1bp)
Condon occupancy(w 1118)
Pearson
r = 0.974
P < 0.001
I
UCC (Ser)
KS test
P-value: 6.909e-33
J
GAC (Asp)
KS test
P-value: 4.593e-41
K
GAU (Asp)
KS test
P-value: 3.502e-47
L
D (Asp)
KS test
P-value: 2.907e-81
Cumulative frequency
Codon A-site occupancy (log2)
Single amino acid A-site occupancy (log2)
M
Normalized RPF counts (log2)
CDS bin position
N
Normalized RPF counts
CDS coordinate
O

Figure S11

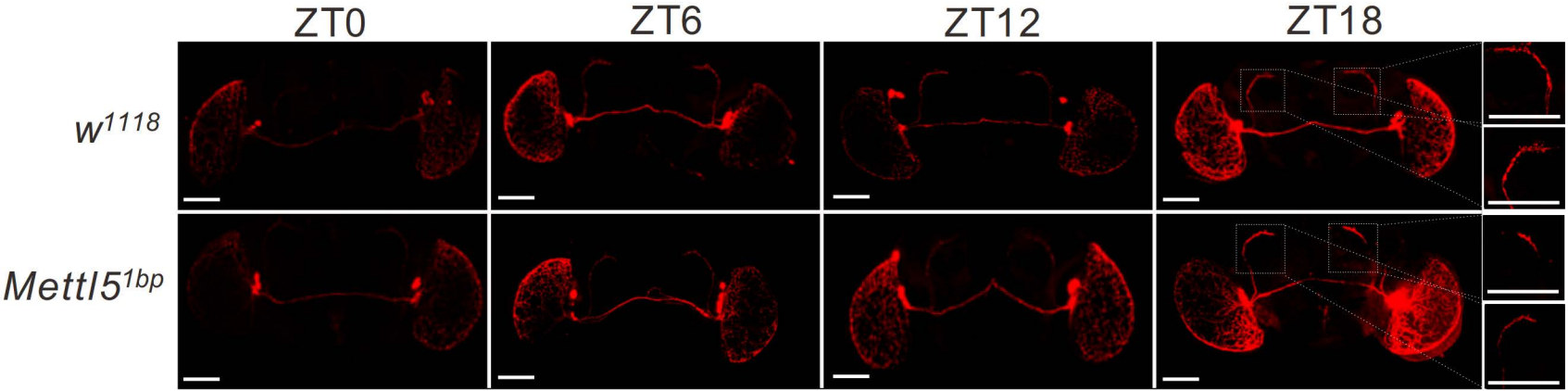

Supplementary figure legends

Figure S1 *Mettl5* functions in a portion of neurons and glia.

(A-C) Colocalization of Mettl5-YFP with antibodies staining ELAV. Scale bar: 50 μm (main figures) and 20 μm (zoomed regions) (D-F) Colocalization of Mettl5-YFP with antibodies staining REPO. Scale bar: 50 μm (main figures) and 20 μm (zoomed regions). (G) Sleep latency. (H) Climbing index of *Mettl5*^{1bp} male flies and control flies. (I) Sleep curves throughout the day for *Mettl5*-RNAi and control flies. (J) Total sleep for *Mettl5*-RNAi and control flies flies. (K) Sleep bout duration of *Mettl5*-RNAi and control flies. (L)Number of sleep bouts of *Mettl5*-RNAi and control flies. For statistical significance, * stands for $p<0.05$, ** stands for $p<0.01$, *** stands for $p<0.001$, *ns* stands for not significant

Figure S2 Quality control of RNA-seq and Ribo-seq samples.

(A, D) Meta analysis of gene expression data obtained from RNA-seq and Ribo-seq. (B, E) Principal component analysis (PCA) of different samples for RNA-seq and Ribo-seq. (C, F) Correlation heatmap of normalized RNA and RPFs values between every pair of samples. The color and size of dots represent the Pearson correlation coefficient.

Figure S3 Heatmap of differentially expressed genes (DEGs) between *Mettl5*^{1bp} and *w*^{1118}.

Heatmap showing the top 100 significantly changed genes identified by RNA-seq (A) and Ribo-seq (B) in *Mettl5*^{1bp}. Red indicates increased expression, while blue indicates decreased expression.

Figure S4 Enrichment analysis of differential expressed genes between *Mettl5*^{1bp} and *w*^{1118}.

(A-D) GO analysis performed on the differentially expressed genes revealed by RNA-seq (A, C) and Ribo-seq (B, D). The bubble chart shows the top 15 most significantly enriched categories under the themes of biological processes, cellular components and molecular functions. The circle color indicates the enrichment p.adjust, and the dot size indicates the number of differentially expressed genes in the functional class or pathway.

Figure S5 Simplified GO enrichment analysis for differentially expressed genes in RNA-seq and Ribo-seq.

GO enrichments for biological process (A, D), cellular components (B, E), and molecular function (C, F) were shown. The bottom right clusters, which lack word cloud annotations, include all other small clusters with fewer than 5 terms. The color shades represent the similarity

of GO terms based on binary cut clustering.

Figure S6 Gene set enrichment analysis (GSEA) for differentially expressed genes found in RNA-seq and Ribo-seq.

GSEA were performed on the differentially expressed genes identified in RNA-seq (A, B) and Ribo-seq (C, D). The top 5 terms or pathways found in GSEA based on GO (A, C) and KEGG (B, D) databases are shown. Genes were sorted according to their signed NES values. The circle color indicates the enrichment p.adjust, and the dot size indicates the number of differentially expressed genes in the respective functional class or pathway.

Figure S7 GO and KEGG enrichment analysis of genes that were significantly changed at both transcriptional and translational levels (showed in figure3L).

(A, B) Top 10 GO and KEGG terms for genes with the same direction of change at transcriptional and translational levels. (C, D) Top 10 GO and KEGG terms for genes with the opposite direction of change at transcriptional and translational levels. (E, F) Top 10 GO terms for genes that were only changed at the transcriptional level; (G, H) Top 10 GO terms for genes that were only changed at the translational level. The circle color indicates the enrichment p.adjust, and the dot size indicates the number of differentially expressed genes in the respective functional class or pathway. Changes with $|\log_2 (\text{fold change})| \geq 0.265$ of translational levels and $|\log_2(\text{fold change})| \geq 1$ of transcriptional levels were considered significant.

Figure S8 TE correlation and P-site offsets

(A-F) TE correlation between the three biological replicates of two group showing high reproducibility. Different colors represent the density distribution of different translated genes. (G-L) Metagene analysis of individual 28nt reads mapped to their 5' ends to determine P-site offsets. The distribution of 28nt RPF reads around the ribosomal P site in w^{1118} (G-I) and *Mettl5* (J-L). The horizontal axis represents the distance from the start-codon or stop-codon, and the vertical axis represents the read counts. The P-site positions are colored according to the reading frame.

Figure S9 Global scan of RPFs distribution

(A-F) Distribution of RPFs periodicity among translation start codons and translation end codons in w^{1118} (A-C) and $Mettl5^{1bp}$ (D-F). (G-L) Distribution of RPFs on different coding frames, including frame 0, frame 1 and frame 2, for the 5'UTR, CDS and 3'UTR in w^{1118} (G-I)

and *Mettl5*^{1bp} (J-L). The plot illustrates the distribution of ribosome-protected fragments (RPFs) across different coding frames (frame 0, frame 1, and frame 2) on the x-axis, with the y-axis representing the percentage of RPFs in each coding frame.

Figure S10 Ribo-seq has revealed that the *Mettl5*^{1bp} leads to changes in global translation features.

(A) The distribution of RPF length among different samples in *Mettl5*^{1bp} and *w*^{1118} was compared. (B) A comparison was made between *Mettl5*^{1bp} and *w*^{1118} regarding the statistics on active translated ORFs. The distribution of different types of ORFs based on their relative location to associated coding sequences (CDS) was illustrated in the comparison between *Mettl5*^{1bp} and *w*^{1118}. The categories include "annotated" (ORFs that overlap with annotated CDS and have the same stop codon as the annotated CDS), "uORF" (ORFs located upstream of annotated CDS , not overlapping annotated CDS), "dORF" (ORFs located downstream of annotated CDS, not overlapping annotated CDS), "Overlap_uORF" (ORFs located upstream of annotated CDS, overlapping annotated CDS), "Overlap_dORF" (ORFs located downstream of annotated CDS, overlapping annotated CDS), "Internal" (ORFs located within annotated CDS but in a different frame relative to the annotated CDS), and "novel" (ORFs located in non-coding genes or non-coding transcripts of coding genes). The percentages of each ORF category were compared between *Mettl5*^{1bp} and *w*^{1118}, providing insights into the differences in ORF distribution between the two analyzed samples. (C) A comparison was made between *Mettl5*^{1bp} and *w*^{1118} regarding the length of translated and untranslated uORFs. (D) The count of dORFs was compared between *Mettl5*^{1bp} and *w*^{1118}. (E) The count of translated uORFs was compared between *Mettl5*^{1bp} and *w*^{1118}. (F, G) Motif analysis was performed separately on the translated and untranslated uORFs between *w*^{1118} and *Mettl5*^{1bp}. (H) The correlation of codon occupancy (A-site) between *Mettl5*^{1bp} and *w*^{1118} was analyzed. (I-L) The cumulative changes in RPFs for codon UCC (I), GAC (J), GAU (K) and amino acid ASP (L) were compared between *Mettl5*^{1bp} and *w*^{1118}. The statistical analysis was performed using the Kolmogorov-Smirnov test (KS test). (M-O) A metagene plot was generated for RPFs on whole CDS region and around the CDS start and end regions in group case study. The CDS was divided into 100 equal bins.

Figure S11 Morphology of clock neurons in *Mettl5* mutant.

Ventral lateral neurons labeled by PDF staining in *Mettl5*^{1bp} and control flies across different

time points.